Available online at www.sciencedirect.com
SCIENCE DIRECT®
Journal of Computational Physics 195 (2004) 202–235
JOURNAL OF COMPUTATIONAL PHYSICS
www.elsevier.com/locate/jcp

Numerical simulation of two-layer shallow water flows through channels with irregular geometry

Manuel J. Castro [a,*], José A. García-Rodríguez [b], José M. González-Vida [a], Jorge Macías [a], Carlos Parés [a], M. Elena Vázquez-Cendón [b]

[a] *Departamento de Análisis Matemático, Universidad de Málaga, 29080, Málaga, Spain*
[b] *Departamento de Matemática Aplicada, Universidad de Santiago de Compostela, 15706, Santiago de Compostela, Spain*

Received 7 March 2003; received in revised form 5 August 2003; accepted 5 August 2003

Abstract

This paper deals with the numerical simulation of flows of stratified fluids through channels with irregular geometry. Channel cross-sections are supposed to be symmetric but not necessarily rectangular. The fluid is supposed to be composed of two shallow layers of immiscible fluids of constant densities, and the flow is assumed to be one-dimensional. Therefore, the equations to be solved are a coupled system composed of two Shallow Water models with source terms involving depth and breadth functions. Extensions of the *Q*-schemes of van Leer and Roe are proposed where a suitable treatment of the coupling and source terms is performed by adapting the techniques developed in [J. Comput. Phys. 148 (1999) 497; Comput. Fluids 29(8) (2000) 17; Math. Model. Numer. Anal. 35(1) (2001) 107]. An enhanced consistency condition, the so-called *C-property*, introduced in [Comput. Fluids 23(8) (1994) 1049] is extended to this case and a general result providing sufficient conditions to ensure this property is shown. Then, some numerical tests to validate the resulting schemes are presented. First we verify that, in practice, the numerical schemes satisfy the *C-property*, even for extremely irregular channels. Then, in order to validate the schemes, we compare some approximate steady solutions obtained with the generalized *Q*-scheme of Van Leer with those obtained by using the asymptotic techniques developed by *Armi and Farmer* for channels with simplified geometries. Finally we apply the numerical scheme to the simulation of the flow through the Strait of Gibraltar. Real bathymetric and coast-line data are considered to include in the model the main features of the abrupt geometry of this natural strait connecting the Atlantic Ocean and the Mediterranean Sea. A steady-state solution is obtained from *lock-exchange* initial conditions. This solution is then used as initial condition to simulate the main semidiurnal and diurnal tidal waves in the Strait of Gibraltar through the imposition of suitable boundary conditions obtained from observed tidal data. Comparisons between numerical results and observed data are also presented.
© 2003 Elsevier Inc. All rights reserved.

Keywords: *Q*-schemes; Coupled conservation laws; Source terms; 1D shallow water equations; Two-layer flows; Hyperbolic systems; Maximal two-layer exchange flows; Strait of Gibraltar; Internal tides

* Corresponding author. Tel.: +34-952-13-18-98; fax: +34-952-13-20-00.
E-mail address: castro@anamat.cie.uma.es (M.J. Castro).

0021-9991/$ - see front matter © 2003 Elsevier Inc. All rights reserved.
doi:10.1016/j.jcp.2003.08.035

1. Introduction

This paper is concerned with the discretization by means of Approximate Riemann Solvers of a P.D.E. system modelling the flow of a stratified fluid along an open channel. The channel is supposed to have a straight axis and to be symmetric with regard to a vertical plane passing through its axis, being channel cross-sections of arbitrary shape. The fluid is assumed to be composed of two shallow layers of immiscible inviscid fluids of constant density. Moreover, we assume that the flow is one dimensional, i.e., at every layer the velocities are uniform over the cross-section and the thickness only depend on the coordinate related to the axis and on time.

This work is a stage of a more general project whose final goal is to obtain a numerical model well suited to study geophysical flows of stratified fluids. This kind of flows frequently appears in applications, such as in estuarine systems, marine density flows, etc. This is the situation, for instance, occurring in the Strait of Gibraltar, where surface water from the Atlantic inflows over saltier westward-flowing Mediterranean water. In this general project, we consider a range of models in increasing order of complexity. It is clear that, in order to obtain realistic simulations of flow exchanges through natural narrows, the final model has to include Coriolis effects, friction, mixing between layer, atmospheric forcing, etc. Moreover, possibly a multi-layer formulation would eventually be required to obtain a more accurate representation of water stratification in some particular cases. Nevertheless, two-layer models can capture some of the most relevant features of this kind of flows and they have frequently been used to study exchange flows through channels connecting two basins with different hydrological characteristics, as it is the case of Gibraltar Narrows (see, for instance, [1,2,9,13,14,20], ...) At the present stage of our project, we consider this kind of models for channels with irregular geometry.

The computation of Shallow Water systems presents some well known difficulties. When the flow is composed of one single layer and the channel has a constant rectangular cross-section, the equations to be solved can be written as a system of conservation laws and standard Approximate Riemann Solvers can be used. When bed elevations or breadth variations are also considered, the equations have the form of a system of conservation laws with source terms or *balance law*. In this case, standard methods can fail in approximating steady or nearly steady flows. In [4,25] the authors have shown that methods based on Approximate Riemann Solvers and *upwinding* of the source terms suitably solve these difficulties. When the flow is composed of two layers, a new difficulty appears related to the coupling terms, which have the form of nonconservative products. In [7] the numerical schemes introduced in [4,25], have been generalized to the system modelling a two-layer flow in a channel with rectangular cross-sections and constant breadth. The aim of this paper is to extend this scheme to the more general situation of channels with irregular geometry and not necessarily rectangular cross-sections.

Thus, the outline of this paper is as follows: In Section 2 model equations are presented. In [8] a system of P.D.E. modelling the flows considered here was deduced, but only the particular case corresponding to a channel with rectangular cross-sections was discretized. In that case, the integral expressions related to the pressure disappear and its treatment becomes simpler. Here, we consider the general case, which is formulated under the form of two coupled systems of conservation laws with source terms, in the sense introduced in [7].

Section 3 is devoted to the construction of the numerical scheme by generalizing the techniques developed in [4,11,21,25,26], for Shallow Water Equations, and those developed in [7,8] for two-layer flows through channels with rectangular cross-sections. The numerical scheme is based on the use of a generalized Q-scheme to discretize the flux terms and an upwinding technique to discretize the source terms. Q-schemes are a family of upwind schemes based on Approximate Riemann Solvers, which are written in flux difference form and whose numerical fluxes are the sum of a centered approximation of the flux function and an upwind term (see [4,5,22–25]). This upwind term is written by means of a *viscosity* matrix Q. In the

particular case of the Q-schemes of Roe and Van Leer considered here, this matrix Q is equal to the absolute value of the matrix of the system evaluated at an *intermediate state*.

In [4] an enhanced consistency condition called *conservation property* or *$\mathscr{C}$-property* was introduced. Numerical schemes satisfying this property can correctly approach steady or nearly steady solutions. In Section 4 we extend the definition of this property to numerical schemes solving the system of equations considered here, and we prove a result giving sufficient conditions for this property to be satisfied. As a corollary, we verify that the Q-schemes of Roe and Van Leer satisfy the conservation property.

In Section 5 we present some numerical experiments. The purpose of these experiments is twofold: On the one hand, to validate the numerical schemes; on the other hand, to decide whether or not this approach is useful for study the exchange flow through the Strait of Gibraltar. Concerning the first purpose, we begin by showing an experiment designed to verify if the $\mathscr{C}$-property is satisfied in practice, even for very irregular geometries. The next two experiments are devoted to test model performance. To do so, we consider channels with rectangular cross-sections and a simple geometry characterized by the presence of a contraction, and the combination of a sill and a contraction. The proposed numerical schemes are applied to these channels in order to obtain stationary solutions that are compared against some steady solutions deduced by using the asymptotic technique developed by *Armi and Farmer* in [1,2]. Finally, to achieve our objective, we consider a channel approaching the real geometry of the Strait of Gibraltar. This is done by constructing from realistic data a symmetric channel which is "equivalent" to the Strait in a sense to be specified. Once this "equivalent channel" is constructed, the model is applied to obtain a steady-state solution as the result of the evolution of the system from *lock-exchange* initial conditions. Then, the main semidiurnal and diurnal tidal waves in the Strait of Gibraltar are simulated. This is done by taking the steady-state solution of the previous experiment as initial condition and imposing the effect of tides through the boundary conditions at the open boundaries. The boundary conditions are constructed from tidal data obtained from [10]. The numerical results are validated against the observed data provided by the same authors and also compared with the synopsis of the essential elements of the time-dependent response of the flow in the Strait of Gibraltar made by Armi and Farmer [3] from observed data collected in April 1986.

Finally, Section 6 is devoted to drawing some concluding remarks and pointing out future lines of research.

2. Governing equations

In [8] the general equations governing the one-dimensional flow of two shallow layers of immiscible fluids along a straight channel with symmetric cross-sections of arbitrary shape were deduced. In this section, and for the sake of completeness, a sketch of the deduction is given but we address the reader to the former reference for further details. Next the system of equations is written under the form of two coupled systems of conservation laws with source terms in the sense introduced in [7].

Let us first introduce some notation. In general, index 1 makes reference to the upper layer and index 2 to the lower one. The coordinate x refers to the axis of the channel; y is the horizontal coordinate normal to the axis; z, the vertical coordinate; and t, the time; g is the gravity; ρ_i is the density of the ith layer ($\rho_1 < \rho_2$), and $r = \rho_1/\rho_2$, their ratio. Variables $b(x)$ and $\sigma(x,z)$ are, respectively, bottom and breadth functions, i.e., channel bottom is defined by the surface of equation $z = b(x)$ and channel walls by the equations: $y = \pm(1/2)\sigma(x,z)$. The variables $A_i(x,t)$ and $h_i(x,t)$ represent the wetted cross-section and the thickness of the ith layer at the section of coordinate x at time t (see Fig. 1(b)), respectively. Therefore A_i and h_i, $i = 1,2$ are related through the equations:

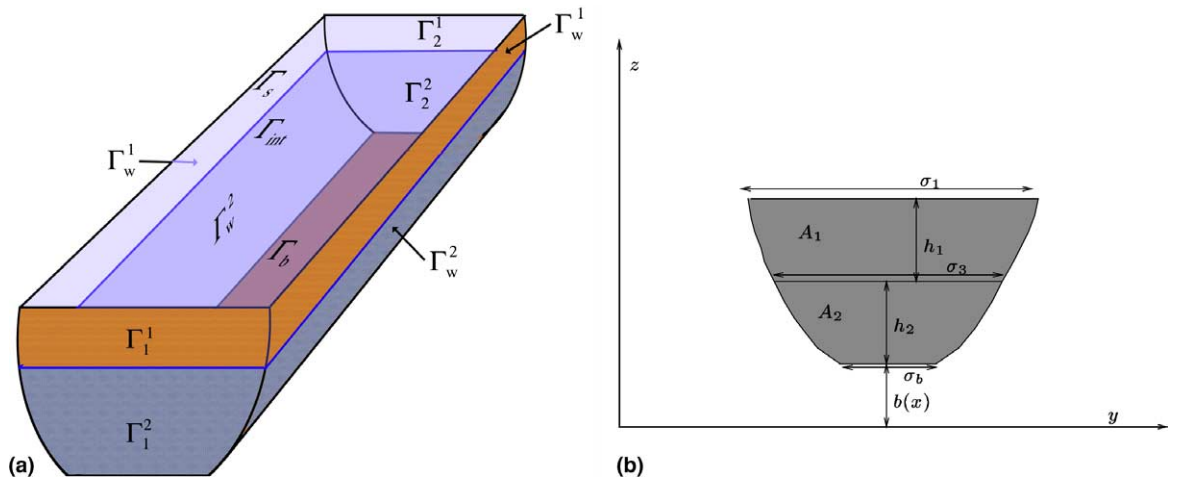

Fig. 1. Notations for a (a) control volume and (b) channel cross-sections.

$$A_1 = \int_{b(x)+h_2}^{b(x)+h_1+h_2} \sigma(x,z)\,\mathrm{d}z, \tag{2.1}$$

$$A_2 = \int_{b(x)}^{b(x)+h_2} \sigma(x,z)\,\mathrm{d}z. \tag{2.2}$$

Finally, $v_i(x,t)$ and $Q_i(x,t) = v_i(x,t)A_i(x,t)$ represent the velocity and the discharge of the ith layer.

Next, we consider a *control volume* of fluid $\mathscr{R}$ which is delimited at time t by two arbitrary cross-sections of coordinates $x = x_1$, $x = x_2$ ($x_1 < x_2$) (see Fig. 1(a)). $\mathscr{R}$ can be decomposed into two volumes, $\mathscr{R}_1$, $\mathscr{R}_2$ each of them corresponding to one layer of fluid. We denote by Γ_1^i, Γ_2^i, $i = 1,2$ the portion of the boundary of $\mathscr{R}_i$ corresponding to the cross-sections $x = x_1$ and $x = x_2$, respectively, and Γ_{w}^i, $i = 1,2$ the boundaries defined by the walls. Finally Γ_{s}, Γ_{int}, and Γ_{b} denote, respectively, the portion of the free surface, interface, and bottom surface between sections $x = x_1$ and $x = x_2$ (see Fig. 1(a)).

The mass conservation law for the ith layer can now be expressed under integral form as follows:

$$\frac{\mathrm{d}}{\mathrm{d}t}\int_{\mathscr{R}_i} \rho_i\,\mathrm{d}V = \rho_i Q_i(x_1,t) - \rho_i Q_i(x_2,t),$$

or, equivalently:

$$\int_{x_1}^{x_2} \rho_i \frac{\partial A_i}{\partial t}(x,t)\,\mathrm{d}x = \int_{x_1}^{x_2} \rho_i \frac{\partial Q_i}{\partial x}(x,t)\,\mathrm{d}x.$$

Next, the first component of the momentum conservation law for the ith layer is expressed also under integral form:

$$\frac{\mathrm{d}}{\mathrm{d}t}\int_{\mathscr{R}_i} \rho_i v_i\,\mathrm{d}V = \rho_i v_i(x_1,t)Q_i(x_1,t) - \rho_i v_i(x_2,t)Q_i(x_2,t) - \int_{\partial\mathscr{R}_i} p_i n_1\,\mathrm{d}\gamma,$$

or

$$\frac{\mathrm{d}}{\mathrm{d}t}\int_{x_1}^{x_2}\rho_i Q_i(x,t)\,\mathrm{d}x = -\int_{x_1}^{x_2}\rho_i\frac{\partial}{\partial x}\frac{Q_i^2}{A_i}(x,t)\,\mathrm{d}x - \int_{\partial\mathscr{R}_i} p_i n_1\,\mathrm{d}\gamma.$$

In this equation, n_1 represents the first component of the outward normal unit vector and p_i is the pressure for the ith layer, which is assumed to be hydrostatic:

$$p_1(x,z) = g\rho_1(b(x)+h_1(x,t)+h_2(x,t)-z) \quad \text{for } b(x)+h_2(x,t)\leqslant z\leqslant b(x)+h_1(x,t)+h_2(x,t);$$
$$p_2(x,z) = g\rho_1 h_1(x,t) + g\rho_2(b(x)+h_2(x,t)-z) \quad \text{for } b(x)\leqslant z\leqslant b(x)+h_2(x,t).$$

Observe that only pressure forces are taken into account as the fluid is supposed to be inviscid. Nevertheless, vertical viscous effects can be easily included into the model by adding parameterizations of the friction forces due to the wind, walls, bottom or friction between layers. In this case, the corresponding source terms appearing in the equations are treated in the same way as in the case of a channel with rectangular cross-sections studied in [7]. Therefore, in order to avoid an excess of notation, we will not include these terms here. Finally notice that the atmospherical pressure has also assumed to be constant and it is set to zero.

The pressure terms for the first layer are as follows:

$$\int_{\Gamma_1^1} p_1 n_1 = -g\rho_1 I_{1,1}(x_1,t),$$

$$\int_{\Gamma_2^1} p_1 n_1 = g\rho_1 I_{1,1}(x_2,t),$$

$$\int_{\Gamma_w^1} p_1 n_1 = g\rho_1\int_{x_1}^{x_2} I_{2,1}(x,t)\,\mathrm{d}x,$$

$$\int_{\Gamma_s} p_1 n_1 = 0,$$

$$\int_{\Gamma_{\mathrm{int}}} p_1 n_1 = -g\rho_1\int_{x_1}^{x_2} h_1\sigma(x,b+h_2)\frac{\partial}{\partial x}(b+h_2)\,\mathrm{d}x,$$

where

$$I_{1,1}(x,t) = \int_{b(x)+h_2(x,t)}^{b(x)+h_1(x,t)+h_2(x,t)} [b(x)+h_1(x,t)+h_2(x,t)-z]\sigma(x,z)\,\mathrm{d}z, \tag{2.3}$$

$$I_{2,1}(x,t) = \int_{b(x)+h_2(x,t)}^{b+h_1(x,t)+h_2(x,t)} [b(x)+h_1(x,t)+h_2(x,t)-z]\frac{\partial\sigma}{\partial x}(x,z)\,\mathrm{d}z. \tag{2.4}$$

For the second layer, we have:

$$\int_{\Gamma_1^2} p_2 n_1 = -g\rho_1 h_1(x_1,t)A_2(x_1,t) - g\rho_2 I_{1,2}(x_1,t),$$

$$\int_{\Gamma_2^2} p_2 n_1 = g\rho_1 h_1(x_2,t)A_2(x_2,t) + g\rho_2 I_{1,2}(x_2,t),$$

$$\int_{\Gamma_w^2} p_2 n_1 = g\rho_1 \int_{x_1}^{x_2} h_1(x,t) I_{3,2}(x,t)\,\mathrm{d}x + g\rho_2 \int_{x_1}^{x_2} I_{2,2}(x,t)\,\mathrm{d}x,$$

$$\int_{\Gamma_b} p_2 n_1 = -g \int_{x_1}^{x_2} (\rho_1 h_1(x,t) + \rho_2 h_2(x,t))\sigma(x,b)\frac{\mathrm{d}b}{\mathrm{d}x},$$

$$\int_{\Gamma_{\mathrm{int}}} p_2 n_1 = g\rho_1 \int_{x_1}^{x_2} h_1 \sigma(x, b+h_2)\frac{\partial}{\partial x}(b+h_2)\,\mathrm{d}x,$$

where

$$I_{1,2}(x,t) = \int_{b(x)}^{b(x)+h_2(x,t)} (b(x) + h_2(x,t) - z)\sigma(x,z)\,\mathrm{d}z, \tag{2.5}$$

$$I_{2,2}(x,t) = \int_{b(x)}^{b(x)+h_2(x,t)} (b(x) + h_2(x,t) - z)\frac{\partial \sigma}{\partial x}(x,z)\,\mathrm{d}z, \tag{2.6}$$

$$I_{3,2}(x,t) = \int_{b(x)}^{b(x)+h_2(x,t)} \frac{\partial \sigma}{\partial x}(x,z)\,\mathrm{d}z. \tag{2.7}$$

The resulting equations can be written in differential form as:

$$\frac{\partial A_1}{\partial t} + \frac{\partial Q_1}{\partial x} = 0, \tag{2.8}$$

$$\frac{\partial Q_1}{\partial t} + \frac{\partial}{\partial x}\left(\frac{Q_1^2}{A_1} + gI_{1,1}\right) = gI_{2,1} - gh_1\sigma(x, b+h_2)\frac{\partial}{\partial x}(b+h_2), \tag{2.9}$$

$$\frac{\partial A_2}{\partial t} + \frac{\partial Q_2}{\partial x} = 0, \tag{2.10}$$

$$\begin{aligned}\frac{\partial Q_2}{\partial t} + \frac{\partial}{\partial x}\left(\frac{Q_2^2}{A_2} + gI_{1,2}\right) = {} & -rgh_1\frac{\partial A_2}{\partial x} - grA_2\frac{\partial h_1}{\partial x} + rgh_1 I_{3,2} + gI_{2,2} \\ & - g(rh_1 + h_2)\sigma(x,b)\frac{\mathrm{d}b}{\mathrm{d}x} + rgh_1\sigma(x, b+h_2)\frac{\partial}{\partial x}(b+h_2).\end{aligned}$$

In the following two subsections, we rewrite the momentum equations in order to express every term as a function of the variables A_i, Q_i, $i = 1, 2$ and their derivatives.

2.1. Momentum equation for the upper layer

First the term $\partial/\partial x(gI_{1,1})$ is written as a function of A_i and Q_i, $i = 1, 2$ by using Leibnitz's Rule:

$$\begin{aligned}\partial I_{1,1}x &= \frac{\partial}{\partial x}\int_{b+h_2}^{b+h_1+h_2}[b(x)+h_1(x,t)+h_2(x,t)-z]\sigma(x,z)\,\mathrm{d}z \\ &= \int_{b+h_2}^{b+h_1+h_2}\frac{\partial}{\partial x}[(b(x)+h_1(x,t)+h_2(x,t)-z)\sigma(x,z)]\,\mathrm{d}z - h_1(x,t)\sigma_3(x,t)\frac{\partial}{\partial x}(b(x)+h_2(x,t)) \\ &= \left[\frac{\mathrm{d}b}{\mathrm{d}x}(x)+\frac{\partial}{\partial x}(h_1(x,t)+h_2(x,t))\right]A_1(x,t)+I_{2,1}(x,t)-h_1(x,t)\sigma_3(x,t)\frac{\partial}{\partial x}(b(x)+h_2(x,t)),\end{aligned} \tag{2.11}$$

where

$$\sigma_3(x,t) = \sigma(x, b(x)+h_2(x,t)) \tag{2.12}$$

is the channel breadth at the interface (see Fig. 1(b)).

In order to avoid an excess of notation, the dependency on x and t will be explicitly written only when necessary to prevent any possible ambiguity.

The next step consists in writing $(\partial/\partial x)h_i$, $i = 1, 2$ in terms of A_i, Q_i, $i = 1, 2$. To do so, the equality (2.1) is differentiated to obtain:

$$\frac{\partial A_1}{\partial x} = I_{3,1}+\sigma_1\frac{\partial h_1}{\partial x}+(\sigma_1-\sigma_3)\frac{\partial}{\partial x}(b+h_2), \tag{2.13}$$

where

$$I_{3,1}(x,t) = \int_{b(x)+h_2(x,t)}^{b+h_1(x,t)+h_2(x,t)}\frac{\partial\sigma}{\partial x}(x,z)\,\mathrm{d}z, \tag{2.14}$$

and

$$\sigma_1(x,t) = \sigma(x, b(x)+h_2(x,t)+h_1(x,t)) \tag{2.15}$$

is the channel breadth at the free surface (see Fig. 1(b)).

Now, from Eq. (2.13), we obtain

$$\frac{\partial h_1}{\partial x} = \frac{1}{\sigma_1}\frac{\partial A_1}{\partial x}-\frac{1}{\sigma_1}\left[I_{3,1}+(\sigma_1-\sigma_3)\frac{\partial}{\partial x}(b+h_2)\right]. \tag{2.16}$$

Similarly, equality (2.2) is differentiated to obtain:

$$\frac{\partial h_2}{\partial x} = \frac{1}{\sigma_3}\frac{\partial A_2}{\partial x}-\frac{1}{\sigma_3}\left[I_{3,2}+(\sigma_3-\sigma_b)\frac{\mathrm{d}b}{\mathrm{d}x}\right], \tag{2.17}$$

where

$$\sigma_b(x) = \sigma(x, b(x)) \tag{2.18}$$

is the channel breadth at the bottom (see Fig. 1(b)).

Now, using expressions (2.11), (2.16), and (2.17), and after some calculations, the following expression for Eq. (2.9) is obtained:

$$\frac{\partial Q_1}{\partial t}+\frac{\partial}{\partial x}\left(\frac{Q_1^2}{A_1}+\frac{g}{2\sigma_1}A_1^2\right) = -\frac{g}{\sigma_1}A_1\frac{\partial A_2}{\partial x}+\frac{g}{2}\left(\frac{1}{\sigma_1}\right)_x A_1^2-g\frac{\mathrm{d}b}{\mathrm{d}x}\frac{\sigma_b}{\sigma_1}A_1+\frac{g}{\sigma_1}(I_{3,1}+I_{3,2})A_1. \tag{2.19}$$

For the sake of simplicity, we do not express the derivative of $1/\sigma_1$ as a function of the derivatives of the unknowns, as its explicit expression is not important for the numerical treatment of this term.

2.2. Momentum equation for the lower layer

Repeating the same procedure than the one used in the previous paragraph, the term $(\partial I_{1,2})/\partial x$ is developed by using the Leibnizt's rule:

$$\frac{\partial I_{1,2}}{\partial x} = \frac{\partial}{\partial x}\int_b^{b+h_2} [b(x)+h_2(x,t)-z]\sigma(x,z)\,\mathrm{d}z = \left[\frac{\mathrm{d}b}{\mathrm{d}x}+\frac{\partial h_2}{\partial x}\right]A_2 + I_{2,2} - h_2\sigma_b\frac{\mathrm{d}b}{\mathrm{d}x}. \tag{2.20}$$

Newly, the use of (2.16) and (2.17) allow us to write (2.11) under the form:

$$\frac{\partial Q_2}{\partial t}+\frac{\partial}{\partial x}\left(\frac{Q_2^2}{A_2}+\frac{g}{2\sigma_2}A_2^2\right) = -r\frac{g}{\sigma_1}A_2\frac{\partial A_1}{\partial x}+\frac{g}{2}\left(\frac{1}{\sigma_2}\right)_x A_2^2 - g\frac{\mathrm{d}b}{\mathrm{d}x}\frac{\sigma_b}{\sigma_2}A_2 + g\left[\frac{r}{\sigma_1}(I_{3,1}+I_{3,2})+\frac{(1-r)}{\sigma_3}I_{3,2}\right]A_2, \tag{2.21}$$

where

$$\frac{1}{\sigma_2} = \frac{1-r}{\sigma_3}+\frac{r}{\sigma_1}, \tag{2.22}$$

and, again, the derivative of $1/\sigma_2$ is not developed in terms of the derivative of the unknowns. Notice that σ_2 has the character of a weighted harmonic mean of σ_1 and σ_3.

2.3. System of equations

Finally, the Eqs. (2.8), (2.19), (2.10), and (2.21) are written as follows:

$$\frac{\partial \mathbf{W}}{\partial t}+\frac{\partial \mathbf{F}}{\partial x}(\boldsymbol{\sigma},\mathbf{W}) = \mathbf{B}(\boldsymbol{\sigma},\mathbf{W})\frac{\partial \mathbf{W}}{\partial x}+\mathbf{V}(\boldsymbol{\sigma},\mathbf{W})+\mathbf{S}(x,\boldsymbol{\sigma},\mathbf{W}), \tag{2.23}$$

where

$$\mathbf{W}(x,t) = [A_1(x,t),Q_1(x,t),A_2(x,t),Q_2(x,t)]^{\mathrm{T}}, \tag{2.24}$$

$$\boldsymbol{\sigma}(x,t) = [\sigma_1(x,t),\sigma_2(x,t),\sigma_3(x,t)]^{\mathrm{T}}, \tag{2.25}$$

$$\mathbf{F}(\boldsymbol{\sigma},\mathbf{W}) = \begin{bmatrix} Q_1 \\ \frac{Q_1^2}{A_1}+\frac{g}{2\sigma_1}A_1^2 \\ Q_2 \\ \frac{Q_2^2}{A_2}+\frac{g}{2\sigma_2}A_2^2 \end{bmatrix}, \tag{2.26}$$

$$\mathbf{B}(\boldsymbol{\sigma},\mathbf{W}) = \begin{bmatrix} 0 & 0 & 0 & 0 \\ 0 & 0 & -g\frac{A_1}{\sigma_1} & 0 \\ 0 & 0 & 0 & 0 \\ -gr\frac{A_2}{\sigma_1} & 0 & 0 & 0 \end{bmatrix}, \tag{2.27}$$

$$\mathbf{V}(\boldsymbol{\sigma},\mathbf{W}) = \begin{bmatrix} 0 \\ \frac{g}{2}\left(\frac{1}{\sigma_1}\right)_x A_1^2 \\ 0 \\ \frac{g}{2}\left(\frac{1}{\sigma_2}\right)_x A_2^2 \end{bmatrix}, \tag{2.28}$$

$$\mathbf{S}(x,\boldsymbol{\sigma},\mathbf{W}) = \begin{bmatrix} 0 \\ g\frac{A_1}{\sigma_1}\int_b^{b+h_1+h_2}\frac{\partial\sigma}{\partial x}\,\mathrm{d}z - gA_1\frac{\sigma_b}{\sigma_1}\frac{\mathrm{d}b}{\mathrm{d}x} \\ 0 \\ -g\frac{\sigma_b}{\sigma_2}\frac{\mathrm{d}b}{\mathrm{d}x}A_2 + gA_2\left(\frac{r}{\sigma_1}\int_b^{b+h_1+h_2}\frac{\partial\sigma}{\partial x}\,\mathrm{d}z + \frac{1-r}{\sigma_3}\int_b^{b+h_2}\frac{\partial\sigma}{\partial x}\,\mathrm{d}z\right) \end{bmatrix}. \tag{2.29}$$

3. Numerical scheme

In [7] a numerical scheme based on Approximate Riemann Solvers for general coupled systems of conservation laws with source terms is developed. In this work, the former scheme is applied to the system (2.23) in the particular case where σ is constant, i.e., for channels with constant breadth rectangular cross-sections.

Nevertheless, the general case (2.23) does not fit into the abstract framework developed in the cited work due to the flux dependence on x via the breadth σ. For the case of a single shallow water layer this difficulty has been studied in [11]. In this section these techniques are applied to construct a numerical scheme for (2.23).

3.1. Numerical fluxes and coupling terms

Let us consider first the following system, where the source term $\mathbf{S}(x,\boldsymbol{\sigma},\mathbf{W})$ has been dropped:

$$\frac{\partial\mathbf{W}}{\partial t} + \frac{\partial\mathbf{F}}{\partial x}(\boldsymbol{\sigma},\mathbf{W}) = \mathbf{B}(\boldsymbol{\sigma},\mathbf{W})\frac{\partial\mathbf{W}}{\partial x} + \mathbf{V}(\boldsymbol{\sigma},\mathbf{W}). \tag{3.1}$$

It is easy to verify that, in matrix form, this system reads as follows:

$$\mathbf{W}_t + \mathscr{A}(\boldsymbol{\sigma},\mathbf{W})\mathbf{W}_x = \mathbf{0}, \tag{3.2}$$

where $\mathscr{A}$ is the 4×4 matrix whose expression is given by:

$$\mathscr{A}(\boldsymbol{\sigma},\mathbf{W}) = \mathbf{J}(\boldsymbol{\sigma},\mathbf{W}) - \mathbf{B}(\boldsymbol{\sigma},\mathbf{W}),$$

with:

$$\mathbf{J}(\boldsymbol{\sigma},\mathbf{W}) = \begin{bmatrix} 0 & 1 & 0 & 0 \\ -\frac{Q_1^2}{A_1^2} + \frac{g}{\sigma_1}A_1 & 2\frac{Q_1}{A_1} & 0 & 0 \\ 0 & 0 & 0 & 1 \\ 0 & 0 & -\frac{Q_2^2}{A_2^2} + \frac{g}{\sigma_2}A_2 & 2\frac{Q_2}{A_2} \end{bmatrix}.$$

Observe that the term $\mathbf{V}(\boldsymbol{\sigma},\mathbf{W})$ vanishes when the system is expressed in the form (3.2), as

$$\frac{\partial\mathbf{F}}{\partial x} = \frac{\partial\mathbf{F}}{\partial\mathbf{W}}\mathbf{W}_x + \frac{\partial\mathbf{F}}{\partial\sigma}\sigma_x = \mathbf{J}(\boldsymbol{\sigma},\mathbf{W})\mathbf{W}_x + \mathbf{V}(\boldsymbol{\sigma},\mathbf{W}).$$

The eigenvalues of $\mathscr{A}$ can be classified in two external and two internal eigenvalues. The external eigenvalues, λ_j^{ext}, $j=1,2$ are related to the propagation speed of barotropic perturbations and the internal ones λ_j^{int}, $j=1,2$ to the propagation of baroclinic perturbations. Unfortunately, analytical expressions of the eigenvalues are not available. Nevertheless, in the case $r\cong 1$, a first-order approximation was given in [19]. Attending to the nature of the internal eigenvalues, the flow is said to be *subcritical* if the sign of the

internal eigenvalues differs, *critical* if one of them takes the value zero, otherwise the flow is called *supercritical*. It can be deduced from the expression of the matrix $\mathscr{A}$ that critical, supercritical and subcritical sections can be characterized by sections where $G^2 = 1$, $G^2 > 1$, $G^2 < 1$, respectively, where

$$G^2 = F_1^2 + F_2^2 - (1-r)\frac{\sigma_2}{\sigma_3}F_1^2F_2^2, \tag{3.3}$$

and

$$F_1^2 = \frac{v_1^2}{g'\left(\frac{\sigma_2}{\sigma_3}\right)\left(\frac{A_1}{\sigma_1}\right)}, \quad F_2^2 = \frac{v_2^2}{g'\left(\frac{A_2}{\sigma_3}\right)}. \tag{3.4}$$

In these definitions, $g' = g(1-r)$ is the reduced gravity, and G and F_i, $i = 1,2$ are the appropriate definitions for this case of the *composite Froude number* and the *internal Froude numbers*, respectively.

The internal eigenvalues may become complex corresponding to the development of shear instabilities (see [15] for more details on instabilities on hydraulically controlled flows). Nevertheless, in this work only the case when the matrix $\mathscr{A}$ has 4 different real eigenvalues is considered, i.e., the flow is supposed to be stable and the system hyperbolic. With the numerical scheme presented here unstable flows cannot be simulated. To do so, friction and/or mixing has to be included in the model.

To obtain a numerical scheme for (3.1) we apply Roe's method [17,18] as it was done in [7] for a particular case. To begin with, the space domain is decomposed into M computing cells $I_i = [x_{i-1/2}, x_{i+1/2}]$ for $i = 1$ to M. Although the numerical scheme is effectively thought and used for irregular meshes, for the sake of simplicity, we assume that these cells have a constant size Δx and that $x_{i+1/2} = i\Delta x$. That means that $x_i = (i-1/2)\Delta x$ is the center of the cell I_i. Let Δt be the time step and $t^n = n\Delta t$. The approximation of $\mathbf{W}(x_i, n\Delta t)$ given by the numerical scheme will be represented by:

$$\mathbf{W}_i^n = \left[A_{i,1}^n,\ Q_{i,1}^n, A_{i,2}^n,\ Q_{i,2}^n\right]^{\mathrm{T}}.$$

The same notation is used for the approximated velocities:

$$u_{i,j}^n = \frac{Q_{i,j}^n}{A_{i,j}^n}, \quad j = 1,2.$$

Once the solution has been computed at the time t^n, the calculation of $\mathbf{W}_i^{n+1}$ requires the choice of an 'intermediate state' between $\mathbf{W}_i^n$ and $\mathbf{W}_{i+1}^n$ at the intercell $x_{i+1/2}$, that is used to linearize the system. This intermediate state will be denoted by

$$\widetilde{\mathbf{W}}_{i+1/2}^n = \left[\tilde{A}_{i+1/2,1}^n,\ \tilde{Q}_{i+1/2,1}^n,\ \tilde{A}_{i+1/2,2}^n,\ \tilde{Q}_{i+1/2,2}^n\right]^{\mathrm{T}}.$$

$\tilde{h}_{i+1/2,j}$, $j = 1,2$ are the thickness related to $\tilde{A}_{i+1/2,j}$, $j = 1,2$ through (2.1), (2.2), and $\widetilde{\boldsymbol{\sigma}}_{i+1/2}^n$ represents the value of $\boldsymbol{\sigma}$ related to $\tilde{h}_{i+1/2,j}$, $j = 1,2$ and $x_{i+1/2}$ through (2.12), (2.15) and (2.22). Finally, $\widetilde{\mathscr{A}}_{i+1/2}$ and $\widetilde{\mathbf{B}}_{i+1/2}$ will denote the value of the matrices $\mathscr{A}$ and $\mathbf{B}$, respectively, corresponding to $\widetilde{\boldsymbol{\sigma}}_{i+1/2}^n$ and $\widetilde{\mathbf{W}}_{i+1/2}^n$.

In the description of the numerical scheme we will use the following matrices:

$$\boldsymbol{\Lambda}_{i+1/2} = \begin{bmatrix} \lambda_{i+1/2,1} & & 0 \\ & \ddots & \\ 0 & & \lambda_{i+1/2,4} \end{bmatrix},$$

whose diagonal coefficients are the eigenvalues of $\widetilde{\mathscr{A}}_{i+1/2}$. By $\mathbf{K}_{i+1/2}$ we denote a matrix whose columns are eigenvectors corresponding to these eigenvalues. The following matrices will also be used:

$$\operatorname{sgn}(\mathbf{\Lambda}_{i+1/2}) = \begin{bmatrix} \operatorname{sgn}(\lambda_{i+1/2,1}) & & 0 \\ & \ddots & \\ 0 & & \operatorname{sgn}(\lambda_{i+1/2,4}) \end{bmatrix}, \quad \mathbf{\Lambda}^{\pm}_{i+1/2} = \begin{bmatrix} (\lambda_{i+1/2,1})^{\pm} & & 0 \\ & \ddots & \\ 0 & & (\lambda_{i+1/2,4})^{\pm} \end{bmatrix},$$

$$\widetilde{\mathscr{A}}^{\pm}_{i+1/2} = \mathbf{K}_{i+1/2}\mathbf{\Lambda}^{\pm}_{i+1/2}\mathbf{K}^{-1}_{i+1/2}, \quad \left|\widetilde{\mathscr{A}}_{i+1/2}\right| = \widetilde{\mathscr{A}}^{+}_{i+1/2} - \widetilde{\mathscr{A}}^{-}_{i+1/2}.$$

Once the intermediate states are chosen, Roe's method is applied in the usual way by solving the linearized Riemann Problems at each interface and integrating on the cells. The numerical scheme obtained can be written as follows:

$$\mathbf{W}^{n+1}_i = \mathbf{W}^n_i + \frac{\Delta t}{\Delta x}(\mathbf{g}^+_{i-1/2} - \mathbf{g}^-_{i+1/2}), \tag{3.5}$$

where

$$\mathbf{g}^+_{i-1/2} = \mathbf{F}(\mathbf{W}^n_i) - \widetilde{\mathscr{A}}^+_{i-1/2}\cdot(\mathbf{W}^n_i - \mathbf{W}^n_{i-1}),$$
$$\mathbf{g}^+_{i+1/2} = \mathbf{F}(\mathbf{W}^n_i) + \widetilde{\mathscr{A}}^-_{i+1/2}\cdot(\mathbf{W}^n_{i+1} - \mathbf{W}^n_i).$$

Let us suppose that the intermediate states chosen are:

$$\widetilde{\mathbf{W}}^n_{i+1/2} = \left[\tilde{A}^n_{i+1/2,1},\ \tilde{Q}^n_{i+1/2,1},\ \tilde{A}^n_{i+1/2,2},\ \tilde{Q}^n_{i+1/2,2}\right]^{\mathrm{T}}, \tag{3.6}$$

with

$$\tilde{A}^n_{i+1/2,j} = \frac{A^n_{i,j} + A^n_{i+1,j}}{2}, \quad \tilde{u}^n_{i+1/2,j} = \frac{\sqrt{A^n_{i,j}}u^n_{i,j} + \sqrt{A^n_{i+1,j}}u^n_{i+1,j}}{\sqrt{A^n_{i,j}} + \sqrt{A^n_{i+1,j}}}, \quad \tilde{Q}^n_{i+1/2,j} = \tilde{A}^n_{i+1/2,j}\tilde{u}^n_{i+1/2,j}, \tag{3.7}$$

and the matrix $\widetilde{\mathscr{A}}_{i+1/2}$ is as follows:

$$\widetilde{\mathscr{A}}_{i+1/2} = \widetilde{\mathbf{J}}_{i+1/2} - \widetilde{\mathbf{B}}_{i+1/2}, \tag{3.8}$$

where

$$\widetilde{\mathbf{J}}_{i+1/2} = \begin{bmatrix} 0 & 1 & 0 & 0 \\ -(\tilde{u}^n_{i+1/2,1})^2 + (\tilde{c}^n_{i+1/2,1})^2 & 2\tilde{u}^n_{i+1/2,1} & 0 & 0 \\ 0 & 0 & 0 & 1 \\ 0 & 0 & -(\tilde{u}^n_{i+1/2,2})^2 + (\tilde{c}^n_{i+1/2,2})^2 & 2\tilde{u}^n_{i+1/2,2} \end{bmatrix}, \tag{3.9}$$

$$\tilde{c}^n_{i+1/2,j} = \sqrt{\frac{g}{\tilde{\sigma}^n_{i+1/2,j}}\frac{A^n_{i,j} + A^n_{i+1,j}}{2}}, \tag{3.10}$$

$$\tilde{\sigma}^n_{i+1/2,1} = \frac{\sigma^n_{i,1} + \sigma^n_{i+1,1}}{2}, \quad \tilde{\sigma}^n_{i+1/2,3} = \frac{\sigma^n_{i,3} + \sigma^n_{i+1,3}}{2}, \quad \frac{1}{\tilde{\sigma}^n_{i+1/2,2}} = \frac{1-r}{\tilde{\sigma}^n_{i+1/2,3}} + \frac{r}{\tilde{\sigma}^n_{i+1/2,1}}. \tag{3.11}$$

Observe that this intermediate state corresponds to choose, for each layer, the usual Roe's average for one-layer shallow water systems.

Then some simple computations show that, in this case, the property

$$\widetilde{\mathscr{A}}_{i+1/2}\cdot\left(\mathbf{W}_{i+1}^{n}-\mathbf{W}_{i}^{n}\right)=\mathbf{F}(\mathbf{W}_{i+1}^{n})-\mathbf{F}(\mathbf{W}_{i}^{n})-\widetilde{\mathbf{V}}_{i+1/2}-\widetilde{\mathbf{B}}_{i+1/2}\left(\mathbf{W}_{i+1}^{n}-\mathbf{W}_{i}^{n}\right),\tag{3.12}$$

is satisfied, where

$$\widetilde{\mathbf{V}}_{i+1/2}=\begin{bmatrix}0\\ \widetilde{V}_{i+1/2,1}\\ 0\\ \widetilde{V}_{i+1/2,2}\end{bmatrix},$$

$$\widetilde{V}_{i+1/2,j}=\frac{g}{2}\left(\frac{1}{\sigma_{i+1,j}}-\frac{1}{\widetilde{\sigma}_{i+1/2,j}}\right)(A_{i+1,j}^{n})^{2}+\frac{g}{2}\left(\frac{1}{\widetilde{\sigma}_{i+1/2,j}}-\frac{1}{\sigma_{i,j}}\right)(A_{i,j}^{n})^{2},\quad j=1,2.\tag{3.13}$$

Then scheme (3.5) writes, thanks to the verification of property (3.12) for Roe's intermediate state (3.6)–(3.10), under the form:

$$\begin{aligned}\mathbf{W}_{i}^{n+1}=\mathbf{W}_{i}^{n}&+\frac{\Delta t}{\Delta x}\left(\mathbf{F}_{i-1/2}-\mathbf{F}_{i+1/2}\right)+\frac{\Delta t}{2\Delta x}\left(\widetilde{\mathbf{B}}_{i-1/2}\cdot(\mathbf{W}_{i}^{n}-\mathbf{W}_{i-1}^{n})+\widetilde{\mathbf{B}}_{i+1/2}\cdot(\mathbf{W}_{i+1}^{n}-\mathbf{W}_{i}^{n})\right)\\&+\frac{\Delta t}{2\Delta x}\left(\widetilde{\mathbf{V}}_{i-1/2}+\widetilde{\mathbf{V}}_{i+1/2}\right),\end{aligned}\tag{3.14}$$

with

$$\mathbf{F}_{i+1/2}=\frac{1}{2}\left(\mathbf{F}(\boldsymbol{\sigma}_{i}^{n},\mathbf{W}_{i}^{n})+\mathbf{F}(\boldsymbol{\sigma}_{i+1}^{n},\mathbf{W}_{i+1}^{n})\right)-\frac{1}{2}\left|\widetilde{\mathscr{A}}_{i+1/2}\right|\cdot(\mathbf{W}_{i+1}^{n}-\mathbf{W}_{i}^{n}).\tag{3.15}$$

This is in fact the general writing of a Q-scheme for solving (3.1). The particular cases are defined by the specific choice of the matrices $\mathscr{A}_{i+1/2}$. In this work, we only consider the Q-scheme of Roe, defined by the choice (3.6)–(3.10) and the Q-scheme of Van Leer, where the intermediate states are defined by

$$\widetilde{\mathbf{W}}_{i+1/2}^{n}=\frac{\mathbf{W}_{i}^{n}+\mathbf{W}_{i+1}^{n}}{2}\tag{3.16}$$

and

$$\mathscr{A}_{i+1/2}=\mathscr{A}\left(\widetilde{\boldsymbol{\sigma}}_{i+1/2}^{n},\widetilde{\mathbf{W}}_{i+1/2}^{n}\right).\tag{3.17}$$

3.2. Source terms

It is known that, when solving shallow water systems, numerical schemes based on centered discretizations can fail in approximating steady flows. In [4,25], a suitable upwinding discretization was introduced to prevent the appearance of this difficulty. Following these authors, we propose the following numerical scheme to solve (2.23):

$$\begin{aligned}\mathbf{W}_{i}^{n+1}=\mathbf{W}_{i}^{n}&+\frac{\Delta t}{\Delta x}\left(\mathbf{F}_{i-1/2}-\mathbf{F}_{i+1/2}\right)+\frac{\Delta t}{2\Delta x}\left(\widetilde{\mathbf{B}}_{i-1/2}\cdot(\mathbf{W}_{i}^{n}-\mathbf{W}_{i-1}^{n})+\widetilde{\mathbf{B}}_{i+1/2}\cdot(\mathbf{W}_{i+1}^{n}-\mathbf{W}_{i}^{n})\right)\\&+\frac{\Delta t}{2\Delta x}\left(\widetilde{\mathbf{V}}_{i-1/2}+\widetilde{\mathbf{V}}_{i+1/2}\right)+\frac{\Delta t}{\Delta x}\left(\mathbf{P}_{i-1/2}^{+}\widetilde{\mathbf{S}}_{i-1/2}+\mathbf{P}_{i+1/2}^{-}\widetilde{\mathbf{S}}_{i+1/2}\right),\end{aligned}\tag{3.18}$$

where

$$\mathbf{P}^{\pm}_{i+1/2} = \tfrac{1}{2}\mathbf{K}_{i+1/2}\big(\mathbf{Id} \pm \operatorname{sgn}(\mathbf{\Lambda}_{i+1/2})\big)\mathbf{K}^{-1}_{i+1/2}, \tag{3.19}$$

and $\widetilde{\mathbf{S}}_{i+1/2}$ is an approximation of the integral of the source term $\mathbf{S}$ at $[x_i, x_{i+1}]$. Here we propose a suitable expression for the numerical treatment of the source terms $\widetilde{\mathbf{S}}_{i+1/2}$.

Remind that the expression of the source term (2.29) is as follows:

$$\mathbf{S}(\boldsymbol{\sigma}, \mathbf{W}) = \begin{bmatrix} 0 \\ \mathbf{S}_{[2]} \\ 0 \\ \mathbf{S}_{[4]} \end{bmatrix},$$

with

$$\mathbf{S}_{[2]} = g\frac{A_1}{\sigma_1}\int_b^{b+h_1+h_2} \frac{\partial \sigma}{\partial x}\,\mathrm{d}z - gA_1\frac{\sigma_b}{\sigma_1}\frac{\mathrm{d}b}{\mathrm{d}x}, \tag{3.20}$$

$$\mathbf{S}_{[4]} = -g\frac{\sigma_b}{\sigma_2}\frac{\mathrm{d}b}{\mathrm{d}x}A_2 + gA_2\left(\frac{r}{\sigma_1}\int_b^{b+h_1+h_2}\frac{\partial \sigma}{\partial x}\,\mathrm{d}z + \frac{1-r}{\sigma_3}\int_b^{b+h_2}\frac{\partial \sigma}{\partial x}\,\mathrm{d}z\right). \tag{3.21}$$

The main difficulty in approximating this source term comes from the integrals appearing in its expression. To deal with this difficulty, we first rewrite $\mathbf{S}$ in such a way that these integrals disappear.

First, from the definition of A_1 and A_2 (see (2.1) and (2.2)) and using Leibnitz's Rule, we obtain:

$$\frac{\partial}{\partial x}(A_1 + A_2) = \frac{\partial}{\partial x}\int_b^{b+h_1+h_2}\sigma(x,z)\,\mathrm{d}z = \int_b^{b+h_1+h_2}\frac{\partial \sigma}{\partial x}\,\mathrm{d}z + \left(\frac{\mathrm{d}b}{\mathrm{d}x} + \frac{\partial h_1}{\partial x} + \frac{\partial h_2}{\partial x}\right)\sigma_1 - \frac{\mathrm{d}b}{\mathrm{d}x}\sigma_b. \tag{3.22}$$

Using this equality, $\mathbf{S}_{[2]}$ can be rewritten as follows:

$$\mathbf{S}_{[2]} = g\frac{A_1}{\sigma_1}\frac{\partial}{\partial x}(A_1 + A_2) - gA_1\frac{\partial}{\partial x}(b + h_1 + h_2). \tag{3.23}$$

Next, from the definition of A_2 (see (2.2)) and using again Leibnitz's Rule, we obtain

$$\frac{\partial A_2}{\partial x} = \frac{\partial}{\partial x}\int_b^{b+h_2}\sigma(x,z)\,\mathrm{d}z = \int_b^{b+h_2}\frac{\partial \sigma}{\partial x}\,\mathrm{d}z + \left(\frac{\mathrm{d}b}{\mathrm{d}x} + \frac{\partial h_2}{\partial x}\right)\sigma_3 - \frac{\mathrm{d}b}{\mathrm{d}x}\sigma_b. \tag{3.24}$$

Taking into account the former equality, (3.22), and the definition of σ_2 (2.22), $\mathbf{S}_{[4]}$ can be rewritten as follows:

$$\mathbf{S}_{[4]} = gA_2\left(\frac{1}{\sigma_2}\frac{\partial A_2}{\partial x} + \frac{r}{\sigma_1}\frac{\partial A_1}{\partial x} - \left(\frac{\mathrm{d}b}{\mathrm{d}x} + \frac{\partial h_2}{\partial x}\right) - r\frac{\partial h_1}{\partial x}\right). \tag{3.25}$$

Using (3.23) and (3.25), the integral of the source term on the interval $[x_i, x_{i+1}]$ is approximated by:

$$\widetilde{\mathbf{S}}_{i+1/2} = \begin{pmatrix} 0 \\ \widetilde{S}_{i+1/2,[2]} \\ 0 \\ \widetilde{S}_{i+1/2,[4]}, \end{pmatrix}, \tag{3.26}$$

where

$$\widetilde{S}_{i+1/2,[2]} = g\widetilde{A}_{i+1/2,1}\left(\frac{1}{\widetilde{\sigma}_{i+1/2,1}}(A_{i+1,1}+A_{i+1,2}-(A_{i,1}+A_{i,2}))-(b_{i+1}+h_{i+1,1}+h_{i+1,2}-(b_i+h_{i,1}+h_{i,2}))\right), \tag{3.27}$$

and

$$\begin{aligned}\widetilde{S}_{i+1/2,[4]} = g\widetilde{A}_{i+1/2,2}\Bigg(&\frac{1}{\widetilde{\sigma}_{i+1/2,2}}(A_{i+1,2}-A_{i,2})+\frac{r}{\widetilde{\sigma}_{i+1/2,1}}(A_{i+1,1}-A_{i,1})\\ &-(b_{i+1}+rh_{i+1,1}+h_{i+1,2}-(b_i+rh_{i,1}+h_{i,2}))\Bigg).\end{aligned} \tag{3.28}$$

3.3. CFL condition and Harten regularization

In the deduction of the schemes CFL-like requirements have to be imposed (see [17]). In practice, we propose the following condition:

$$\max\left\{|\lambda_{i+1/2,l}| \mid 1\leqslant l\leqslant 4,\ 1\leqslant i\leqslant M\right\}\frac{\Delta t}{\Delta x}\leqslant\gamma,$$

where $0<\gamma\leqslant 1$ is the CFL number.

In general, the numerical scheme can run with CFL numbers close to 1: restrictions on the CFL number are only required when there are fronts separating one layer or two layer flows, as is the case in lock-exchange experiments (see Section 5).

Finally, in order to prevent the numerical viscosity of the Q-schemes from vanishing when any of the eigenvalues of the matrices $|\widetilde{\mathscr{A}}_{i+1/2}|$ are zero, we apply Harten regularization [12].

3.4. Some remarks about the numerical implementation

The implementation of the numerical schemes introduced above presents some practical difficulties. The first one is related to the calculation of the thickness h_i, $i=1,2$. More precisely, the problem consists in given the values $A^n_{l,1}$ and $A^n_{l,2}$ of the wetted cross-sections at the cell I_l how to calculate $h^n_{l,j}$, $j=1,2$ defined by the relationships:

$$A^n_{l,1}=\int_{b_l+h^n_{l,2}}^{b_l+h^n_{l,1}+h^n_{l,2}}\sigma(x_l,z)\,\mathrm{d}z, \tag{3.29}$$

$$A^n_{l,2}=\int_{b_l}^{b_l+h^n_{l,2}}\sigma(x_l,z)\,\mathrm{d}z, \tag{3.30}$$

where x_l is the center of the cell and $b_l=b(x_l)$. To solve this problem, we first construct a continuous linear piece-wise approximation Σ_l of the function $\sigma(x_l,\cdot)$ as follows: Given $z\in[b_l,\infty)$

$$\Sigma_l(z)=\begin{cases}\sigma(x_l,b_l+H_{l,j+1})\frac{z-b_l-H_{l,j}}{H_{l,j+1}-H_{l,j}}-\sigma(x_l,b_l+H_{l,j})\frac{z-b_l-H_{l,j+1}}{H_{l,j+1}-H_{l,j}}, & \text{if } H_{l,j}\leqslant z-b_l\leqslant H_{l,j+1},\\ & \quad j=0,\ldots,P-2,\\ \sigma(x_l,b_l+H_{l,P})\frac{z-b_l-H_{l,P-1}}{H_{l,P}-H_{l,P-1}}-\sigma(x_l,b_l+H_{l,P-1})\frac{z-b_l-H_{l,P}}{H_{l,P}-H_{l,P-1}}, & \text{if } H_{l,P-1}\leqslant z-b_l,\end{cases}$$

where $H_{l,0}=0$ and $\{H_{l,1},\ldots,H_{l,P}\}$ are P values previously chosen. Then, we approximate $h^n_{l,j}$, $j=1,2$ by the solutions $\tilde{h}_j$, $j=1,2$ of the problems:

$$A^n_{l,1} = \int_{b_l+\tilde{h}_2}^{b_l+\tilde{h}_1+\tilde{h}_2} \Sigma_l(z)\,\mathrm{d}z, \tag{3.31}$$

$$A^n_{l,2} = \int_{b_l}^{b_l+\tilde{h}_2} \Sigma_l(z)\,\mathrm{d}z. \tag{3.32}$$

To efficiently solve this problem, we first define the values $R_{l,j}$ associated to $H_{l,j}$, $j = 0,\ldots,P$ as

$$R_{l,j} = \int_{b_l}^{b_l+H_{l,j}} \Sigma_l(z)\,\mathrm{d}z, \tag{3.33}$$

which are easily calculated. Notice that the computation of these values has to be performed only once. Now, $\tilde{h}_2$ is computed using the following algorithm:

- Searching for the index j^n such that $R_{l,j^n} \leqslant A^n_{l,2} < R_{l,j^n+1}$ (if $A^n_{l,2} \geqslant R_{l,P}$ then $j^n = P-1$).
- Calculate $\tilde{h}_2$ by:

$$\tilde{h}_2 = \begin{cases} H_{l,j^n} + \dfrac{\sqrt{4\Sigma_l(b_l+H_{l,j^n})^2 + 8(A^n_{l,2}-R_{l,j^n})\alpha} - 2\Sigma_l(b_l+H_{l,j^n})}{2\alpha} & \text{if } \alpha \neq 0, \\ H_{l,j^n} + \dfrac{A^n_{l,2}-R_{l,j^n}}{\Sigma_l(b_l+H_{j^n})} & \text{if } \alpha = 0, \end{cases}$$

where

$$\alpha = \frac{\Sigma_l(b_l+H_{l,j^n+1}) - \Sigma_l(b_l+H_{l,j^n})}{H_{l,j^n+1}-H_{l,j^n}}.$$

To initialize the searching algorithm described above a first initial guess of the index must be done (in practice j^{n-1} is taken) and then the search follows moving upwards or downwards. Once the value for $\tilde{h}_2$ has been found, $\tilde{h}_1$ is a calculated in a similar way: The same algorithm is used, but substituting $A^n_{l,2}$ by $A^n_{l,2} + A^n_{l,1}$.

Finally the approximations of $\sigma_3(x_l, n\Delta t)$ and $\sigma_1(x_l, n\Delta t)$ are given by

$$\sigma^n_{3_l} = \Sigma_l(b_l+\tilde{h}_2) \quad \text{and} \quad \sigma^n_{1_l} = \Sigma_l(b_l+\tilde{h}_2+\tilde{h}_1),$$

respectively.

Another difficulty that appears at the implementation stage is the approximation of the eigenvalues and eigenvectors of the matrices $\mathscr{A}_{i+1/2}$. We have used Laguerre's method for approximating the roots of the characteristic equation $\det(\mathbf{Id} - \lambda A_{i+1/2}) = 0$. In the case $r \sim 1$, as initial guess for the algorithm the first order approximations provided in [19] are used. With this initial choice, in practice, Laguerre's methods only needs 2 or 3 iterations to converge, being the cost of the solution of these spectral problems negligible compared with the computation of the matrices $|\mathscr{A}|$, $P^+_{i+1/2}$, $P^-_{i+1/2}$ appearing in the scheme.

4. Conservation property

In [4] an enhanced consistency condition called *conservation property* or *$\mathscr{C}$-property* was introduced in order to characterize how exactly a numerical scheme approximates a steady solution representing water at rest. In this section, this property is extended to the case under study and we analyze whether or not the numerical schemes introduced in the previous section satisfy the extended condition.

In the context of the present work, a steady-state solution representing water at rest is characterized by (see Fig. 2):

$$Q_1(x) = Q_2(x) = 0, \quad A_1(x) = \int_{\bar{h}_2}^{\bar{h}_2+\bar{h}_1} \sigma(x,z)\,\mathrm{d}z, \quad A_2(x) = \int_{b(x)}^{\bar{h}_2} \sigma(x,z)\,\mathrm{d}z, \tag{4.1}$$

where $\bar{h}_1$ and $\bar{h}_2$ are two constants such that:

$$\bar{h}_1 > 0; \quad \bar{h}_2 \geqslant b(x) \qquad \forall x.$$

The natural extension of the $\mathscr{C}$-property is thus as follows:

Definition 1. It is said that a numerical scheme for solving (2.23) satisfies the $\mathscr{C}$-property, if any steady-state solution given by (4.1) is computed exactly.

The following result holds:

Theorem 1. *Let us consider a numerical scheme of the form* (3.18) *for solving* (2.23)*. Given any steady solution* (A_1, Q_1, A_2, Q_2) *verifying* (4.1)*, we define*

$$\bar{\mathbf{W}}_i = [A_1(x_i);\ Q_1(x_i);\ A_2(x_i);\ Q_2(x_i)]^{\mathrm{T}}. \tag{4.2}$$

If, for each i, the following equalities hold

$$\mathscr{A}_{i+1/2} \cdot \left(\bar{\mathbf{W}}_{i+1} - \bar{\mathbf{W}}_i\right) = \mathbf{F}(\bar{\mathbf{W}}_{i+1}) - \mathbf{F}(\bar{\mathbf{W}}_i) - \widetilde{\mathbf{V}}_{i+1/2} - \widetilde{\mathbf{B}}_{i+1/2}\left(\bar{\mathbf{W}}_{i+1} - \bar{\mathbf{W}}_i\right), \tag{4.3}$$

$$\mathscr{A}_{i+1/2} \cdot \left(\bar{\mathbf{W}}_{i+1} - \bar{\mathbf{W}}_i\right) = \widetilde{\mathbf{S}}_{i+1/2}, \tag{4.4}$$

then the scheme satisfies the $\mathscr{C}$-property.

Proof. To prove the theorem, we apply the numerical scheme to the initial condition

$$\mathbf{W}_i^0 = \bar{\mathbf{W}}_i \quad \forall i.$$

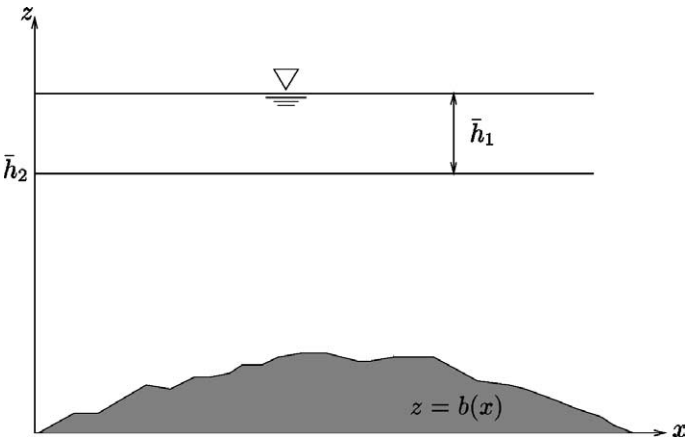

Fig. 2. Longitudinal section of a solution representing water at rest.

Observe that (4.3) is a particular case of (3.12), which is the condition satisfied when Roe's intermediate states have been chosen. Now this condition can be used, as it was done in Section 3.1, but going backwards to write the first stage of the scheme as follows:

$$\mathbf{W}_i^1 = \mathbf{W}_i^0 - \frac{\Delta t}{\Delta x}\left(\mathscr{A}^+_{i-1/2}\cdot(\mathbf{W}_i^0 - \mathbf{W}_{i-1}^0) + \mathscr{A}^-_{i+1/2}\cdot(\mathbf{W}_{i+1}^0 - \mathbf{W}_i^0)\right) + \frac{\Delta t}{\Delta x}\left(\mathbf{P}^+_{i-1/2}\widetilde{\mathbf{S}}_{i-1/2} + \mathbf{P}^-_{i+1/2}\widetilde{\mathbf{S}}_{i+1/2}\right).$$

If we prove that, for every i, the following equalities hold:

$$P^{\pm}_{i+1/2}\widetilde{\mathbf{S}}_{i+1/2} = \mathscr{A}^{\pm}_{i+1/2}\cdot(\mathbf{W}_{i+1}^0 - \mathbf{W}_i^0), \tag{4.5}$$

then

$$\mathbf{W}_i^1 = \mathbf{W}_i^0 \quad \forall i.$$

Now, to prove (4.5) we first need to establish the following matrix identity:

$$\begin{aligned} P^{\pm}_{i+1/2}\mathscr{A}_{i+1/2} &= \frac{1}{2}\mathbf{K}_{i+1/2}\left(\mathbf{Id} \pm \operatorname{sgn}(\mathbf{\Lambda}_{i+1/2})\right)\mathbf{K}^{-1}_{i+1/2}\mathscr{A}_{i+1/2} = \frac{1}{2}\mathbf{K}_{i+1/2}\left(\mathbf{Id} \pm \operatorname{sgn}(\mathbf{\Lambda}_{i+1/2})\right)\mathbf{\Lambda}_{i+1/2}\mathbf{K}^{-1}_{i+1/2} \\ &= \mathbf{K}_{i+1/2}\mathbf{\Lambda}^{\pm}_{i+1/2}\mathbf{K}^{-1}_{i+1/2} = \mathscr{A}^{\pm}_{i+1/2}. \end{aligned}$$

Multiplying (4.4) by the matrix $P^{\pm}_{i+1/2}$ and using the former matrix equality, we obtain (4.5). □

Corollary 1. *If a numerical scheme of the form* (3.18) *with source terms given by* (3.26)–(3.28) *is such that the matrices* $\mathscr{A}_{i+1/2}$ *coincide with those of Roe's method when the scheme is applied to the initial condition* (4.2)*, then it satisfies the* $\mathscr{C}$*-property.*

Proof. First, it is trivial to prove that (4.3) is satisfied if Roe's intermediate states are chosen, as this condition is a particular case of the more general property (3.12) established in Section 3.1 for Roe's states.

On the other hand, an easy computation shows that, in the particular case of the states (4.2) the non-zero components of (3.26) writes as follows:

$$\begin{aligned} \widetilde{S}_{i+1/2,[2]} &= g\widetilde{A}_{i+1/2,1}\frac{1}{\widetilde{\sigma}_{i+1/2,1}}(A_{i+1,1} + A_{i+1,2} - (A_{i,1} + A_{i,2})), \\ \widetilde{S}_{i+1/2,[4]} &= g\widetilde{A}_{i+1/2,2}\left(\frac{1}{\widetilde{\sigma}_{i+1/2,2}}(A_{i+1,2} - A_{i,2}) + \frac{r}{\widetilde{\sigma}_{i+1/2,1}}(A_{i+1,1} - A_{i,1})\right), \end{aligned}$$

and

$$\widetilde{\mathscr{A}}_{i+1/2} = \begin{bmatrix} 0 & 1 & 0 & 0 \\ \frac{g}{\widetilde{\sigma}_{i+1/2,1}}\widetilde{A}_{i+1/2,1} & 0 & \frac{g}{\widetilde{\sigma}_{i+1/2,1}}\widetilde{A}_{i+1/2,1} & 0 \\ 0 & 0 & 0 & 1 \\ \frac{gr}{\widetilde{\sigma}_{i+1/2,1}}\widetilde{A}_{i+1/2,2} & 0 & \frac{g}{\widetilde{\sigma}_{i+1/2,2}}\widetilde{A}_{i+1/2,2} & 0 \end{bmatrix}.$$

From these equalities, (4.4) is trivially obtained.

As a consequence, the methods of Roe and Van Leer with numerical source terms given by (3.26)–(3.28) satisfy the conservation property. □

Remark 1. The Theorem 1 can be easily adapted to the case of the Shallow Water Equations with source terms.

5. Numerical results

In this section, some experiments that illustrate the properties of the proposed numerical schemes are presented. In all the cases, the method of Van Leer is used.

5.1. Water at rest in a channel with irregular geometry and triangular cross-sections

In this subsection, a numerical test is presented to verify how exactly the $\mathscr{C}$-property is, in practice, satisfied for a channel with very irregular geometry. To do this, we considered a channel with triangular cross-sections and for which depth and breadth were randomly generated. Then, the scheme was applied taking as initial condition a steady solution representing water at rest. The CFL parameter is set to 0.9 and $\Delta x = 0.05$. Figs. 3(a) and (b) show bottom topography and upper channel breadth, respectively. Figs. 3(c) and (d) depict the free surface and the interface at the initial time and after 10 seconds of simulation. Finally, Figs. 3(e) and (f) show the value of the discharge at each layer at initial state and after 10 seconds of simulation, respectively. The water elevation at the free surface and at the interface is exactly computed being zero at every time iteration. Nevertheless non-zero discharges appear, but they are of the order of the round-off error unit and they do not grow with time. The time iteration corresponding to $t = 10$ s. have been plotted as example, but the solution at any other time looks exactly the same. As it can be observed in the figures, no spurious waves appear.

5.2. Two-layer exchange flow through a channel with a contraction

The validation of numerical schemes for solving (2.23) is not a simple task, as exact solutions for this system are not easily obtained. Nevertheless, *Armi and Farmer* in [1,2] introduced, in the context of the study of exchange flows through channels, an asymptotic technique to obtain steady solutions for channels with simplified geometries.

The goal of this section is to approximate numerically the so-called *maximal solution* in a channel connecting two infinite basins with water of different densities whose ratio is $r \cong 1$. In this particular test case, channel geometry is defined by a single contraction with a flat bottom and rectangular cross-sections. The numerical solution obtained by this test will be compared against the stationary solutions provided by *Armi and Farmer*. But let us first briefly recall the main aspects of the theory developed by these authors. In their works, smooth steady-state solutions are studied. To do this, the flow of each layer is modelled by using Bernoulli's equation. The *rigid lid* approximation is assumed. The equations are first written in non-dimensional form using some dimensionless variables Q_i', h_i', σ' that are such that $\sigma' = 1$ at the contraction and $h_1' + h_2' = 1$ everywhere (observe that, due to the hypothesis of rigid lid, the sum of the two layers thickness is constant). On the other hand, as the steady-state mass equations reduce to $\partial_x Q_i = 0$, Q_1 and Q_2 (or, equivalently, Q_1' and Q_2') are constants. Let $q_r = |Q_1/Q_2|$ be the ratio of the discharges. Here, only the case $q_r = 1$ will be considered.

If the equations of the two layers are written in terms of the internal Froude numbers, $F_i = v_i/\sqrt{(g'h_i)}$, $i = 1, 2$, and they are subtracted, the following equality is obtained:

$$\frac{F_2^{-2/3}(1 + \frac{1}{2}F_2^2) - \frac{1}{2}q_r^{2/3}F_1^{-2/3}F_1^2}{q_r^{2/3}F_1^{-2/3} + F_2^{-2/3}} = \Delta H'. \tag{5.1}$$

$\Delta H'$ is a constant corresponding to the dimensionless energy difference between the two layers.

The solutions of the equations can be identified by a curve in the (F_1^2, F_2^2)-plane of Froude numbers, this curve is given by Eq. (5.1). These solutions haven been plotted in detail in [1]. In Fig. 4, we show the curves corresponding to the physically feasible steady-state solutions for $q_r = 1$.

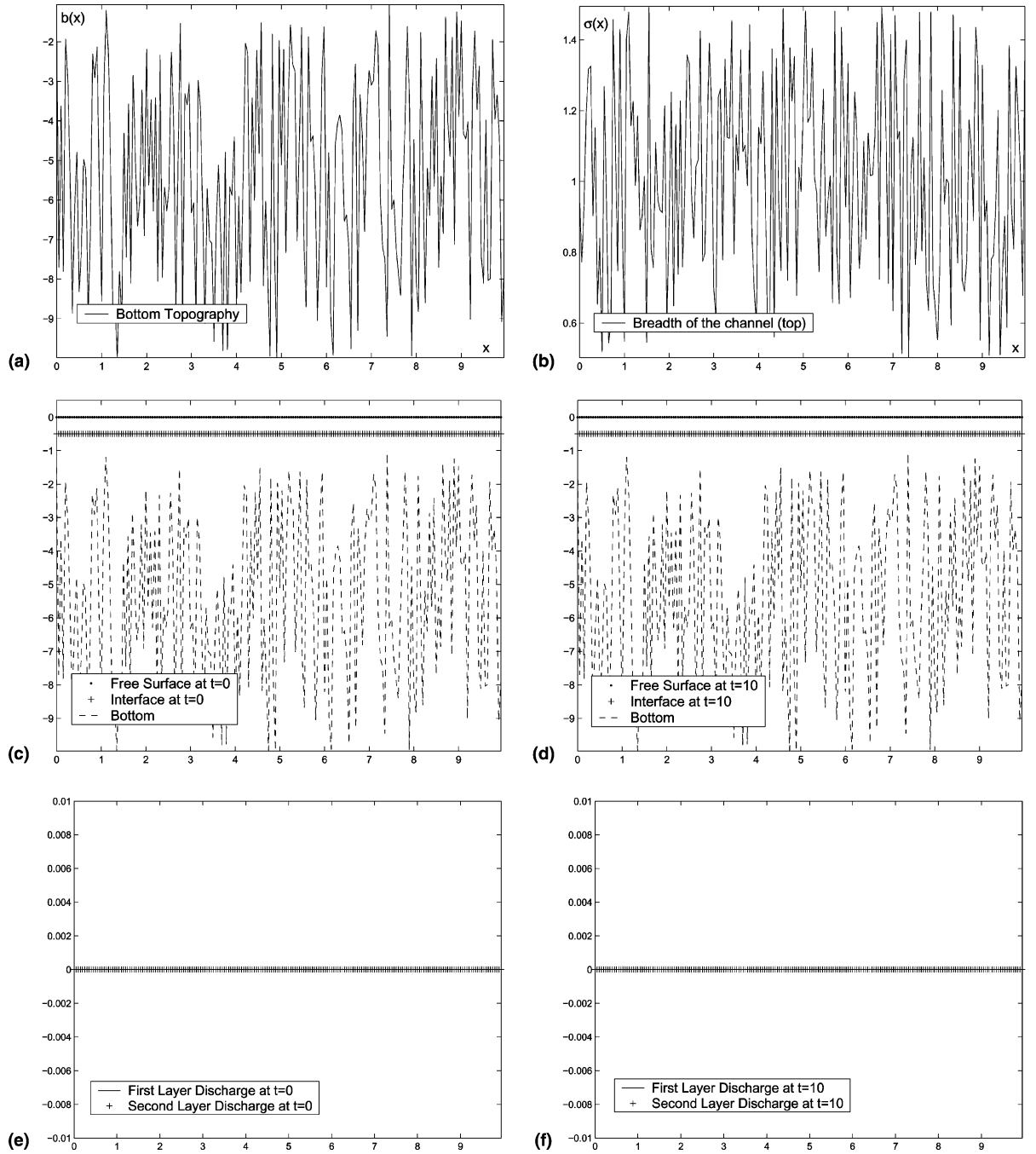

Fig. 3. $\mathscr{C}$-property verification test: water at rest in an irregular channel. (a) Bottom topography (random); (b) channel breath at top (random); (c) free surface and interface at initial state; (d) free surface and interface after 10 s of simulation; (e) discharge at each layer at initial state; (f) discharge at each layer after 10 s of simulation.

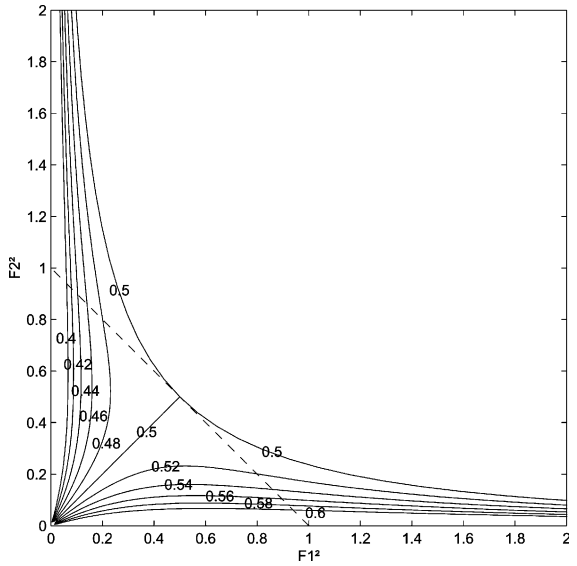

Fig. 4. Solutions to the Bernoulli equations in the Froude-number plane for $q_r = 1$. Each solution curve is labelled with its non-dimensional energy difference between the two layers.

The details of the solution corresponding to one of these curves can be recovered by studying its intersections with the curves of equation:

$$q_r^{2/3} F_1^{-2/3} + F_2^{-2/3} = \left(\frac{Q_2'}{\sigma'} \right)^{-2/3}, \tag{5.2}$$

which is the equality $h_1' + h_2' = 1$ expressed in terms of F_i, $i = 1, 2$. This is done as follows: It can be proved that, if a smooth steady-state solution has a critical section, it is necessarily located at the contraction. As $r \cong 1$, the Composite Froude number can be approximated by:

$$G^2 \cong F_1^2 + F_2^2.$$

Using this approximation, a critical section is characterized by the equation $F_1^2 + F_2^2 = 1$. This equation defines a straight line in the (F_1^2, F_2^2)-plane, also represented in Fig. 4 (dashed line), that separates subcritical from supercritical states. Now let us suppose that the curve corresponding to a solution intersect at a point (F_1^2, F_2^2) with the dashed line. Taking into account that critical sections have to be located at the contraction where $\sigma' = 1$, the value of Q_2' (and, consequently, of Q_1') corresponding to that particular solution can be calculated by using Eq. (5.2). Once the discharges known, all the details of the solution can be easily computed.

The maximal solution is that corresponding to the branch of the $\Delta H' = 0.5$ curve which is on the supercritical region, for which the discharge is maximal. It can be observed that it is the sole solution for which the flow is supercritical everywhere. The other solutions are called *submaximal*. For these solutions, the critical section is located at the contraction and it separates subcritical from supercritical flow. It can be shown that the maximal solution is marginally stable along the entire channel, i.e., the two internal eigenvalues coincide.

Coming back to the numerical experiment, we consider a channel with a length of 6 meters, discretized in 150 cells, whose breadth function is given by (see Fig. 5)

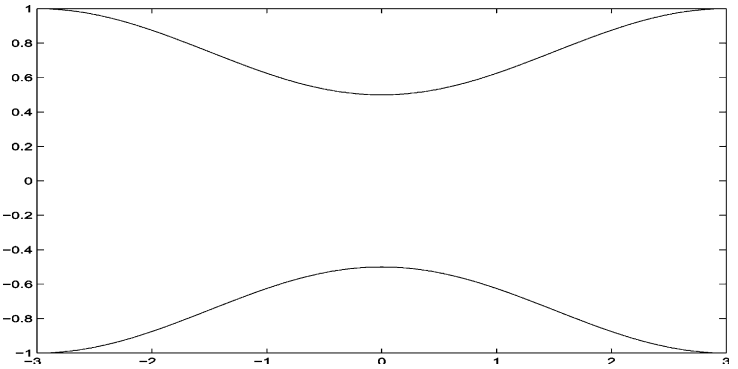

Fig. 5. Sketch showing contraction plan view.

$$\sigma(x) = 2 - \exp(-x^2), \quad x \in [-3, 3],$$

and we consider a *lock-exchange* experiment: As initial state, two fluids of constant densities ρ_1 and ρ_2, with $r = \rho_1/\rho_2 = 0.98$, are at rest and separated by a vertical "artificial barrier" located at the narrowest channel section (see Fig. 6(a)). This barrier is dropped out at time $t = 0$ and the model is integrated until a steady state is reached (see Fig. 6(b)). At the boundaries only the ratio q_r between fluxes is imposed and it is set to 1, i.e., $Q_1 = -Q_2$. In this experiment CFL is set to 0.7. Fig. 6(b) shows the steady state reached which is compared with the corresponding maximal A&F solution: Both curves can not be distinguished. The constant exchange flux predicted by the model is $Q_1 = -Q_2 = 1.111 \times 10^{-1}$ m^3/s while F&A model gives $Q_1 = -Q_2 = 1.107 \times 10^{-1}$ m^3/s.

Notice that the general assumption made in Section 3.1 concerning the flows to be considered in this work is not satisfied for the maximal solution: at any point of the channel the matrix of the system has only 3 real distinct eigenvalues and thus the system is not strictly hyperbolic. In this case, the numerical scheme has been slightly modified: when the numerical method used to solve the spectral problems finds a double internal eigenvalue λ, the matrix $\mathscr{A}$ is perturbed so that it has 4 real distinct eigenvalues: the two external eigenvalues and $\lambda \pm \varepsilon$, for a given ε small. Fig. 7(a) shows the internal eigenvalues along the channel for the

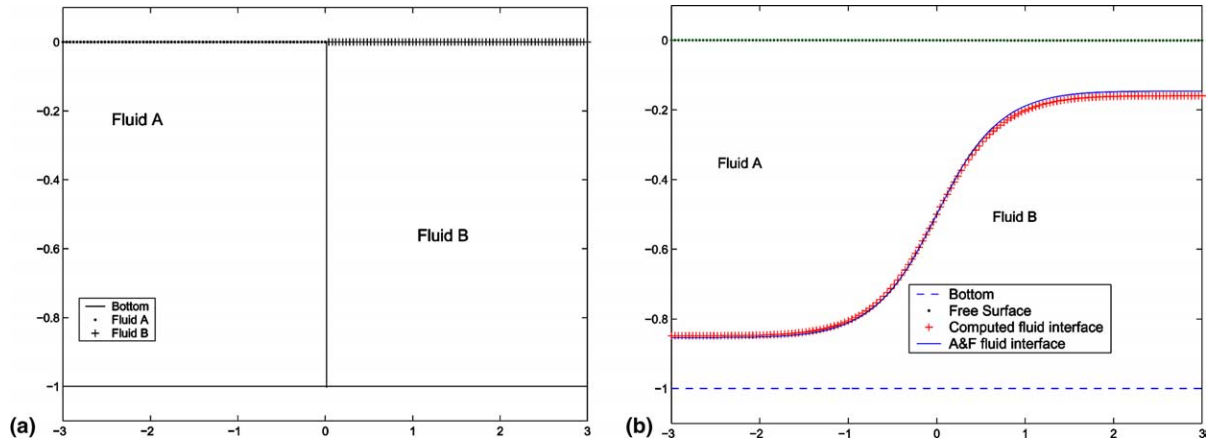

Fig. 6. Maximal exchange flow through a rectangular channel with a contraction. (a) Initial condition and (b) comparison with A&F stationary solution.

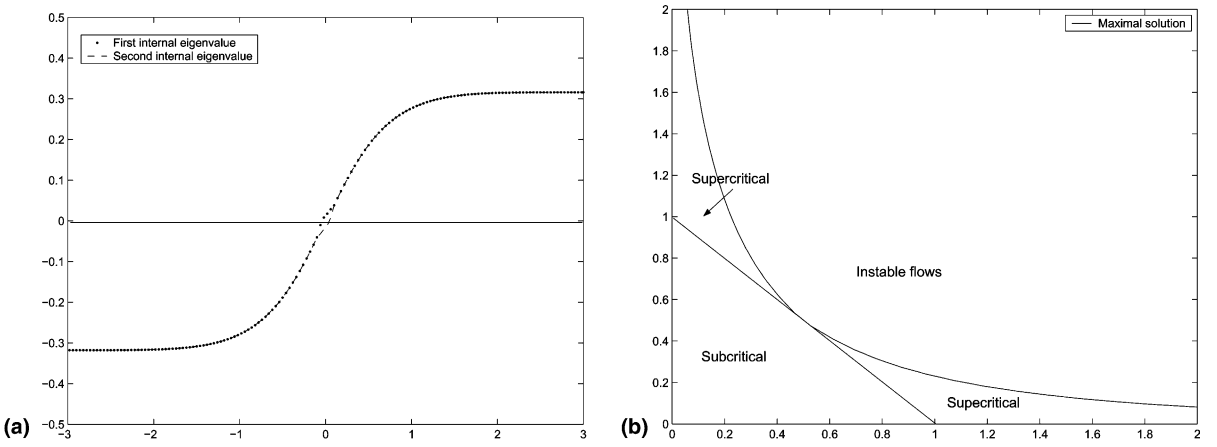

Fig. 7. Internal eigenvalues of the maximal exchange flow for $q_r = 1.0$ and its representation in the Froude-number plane. (a) Internal eigenvalues; (b) maximal solution in the Froude-number plane.

numerical steady-state solution. It can be observed also that the solution is supercritical everywhere but near the contraction, where two critical sections appear linked by a small subcritical region. In fact, this small disturbance is due to the Harten's regularization: at $x = 0$ the internal eigenvalues take the value zero and some numerical viscosity has to be added, otherwise the numerical solution would converge to a solution presenting a non-entropic stationary shock placed at this point. The representation of this numerical solution in the Froude-number plane is shown in Fig. 7(b).

5.3. Two-layer exchange flow through a channel with a sill and a contraction

The techniques developed by *Armi and Farmer* can be generalized to a channel with rectangular cross-section whose geometry presents the combination of an offset sill and a contraction (see [16]). As in the previous example, in this paragraph we use these "generalized A&F solutions" (GA&F hereafter) to validate the steady-state solutions obtained with our numerical scheme.

We consider now a rectangular channel whose geometry is given by the functions (see Fig. 8).

$$b(x) = \frac{1}{\cosh^2(3.75x)}, \quad x \in [-1, 2],$$

$$\sigma(x) = 0.5 + 1.5(1 - \mathrm{e}^{-a^2(x-1)^2}), \quad x \in [-1, 2], \quad a = \begin{cases} 0.637 & \text{if } x \leqslant 1 \\ 1.273 & \text{if } x > 1. \end{cases}$$

They represent a channel with a sill placed at $x = 0$ and a contraction located at $x = 1$ and $\Delta x = 3/200$.

The experiment performed consists in taking

$$\begin{cases} h_1(0,x) = 1.3 - b(x), \\ h_2(0,x) = 0.7, \\ q_1(0,x) = q_2(0,x) = 0, \end{cases}$$

as initial conditions and

$$\begin{cases} q_1(t,2) = q_1^{\mathrm{R}}, \\ q_2(t,-1) = q_2^{\mathrm{L}}, \quad q_2(t,2) = q_2^{\mathrm{R}}, \end{cases}$$

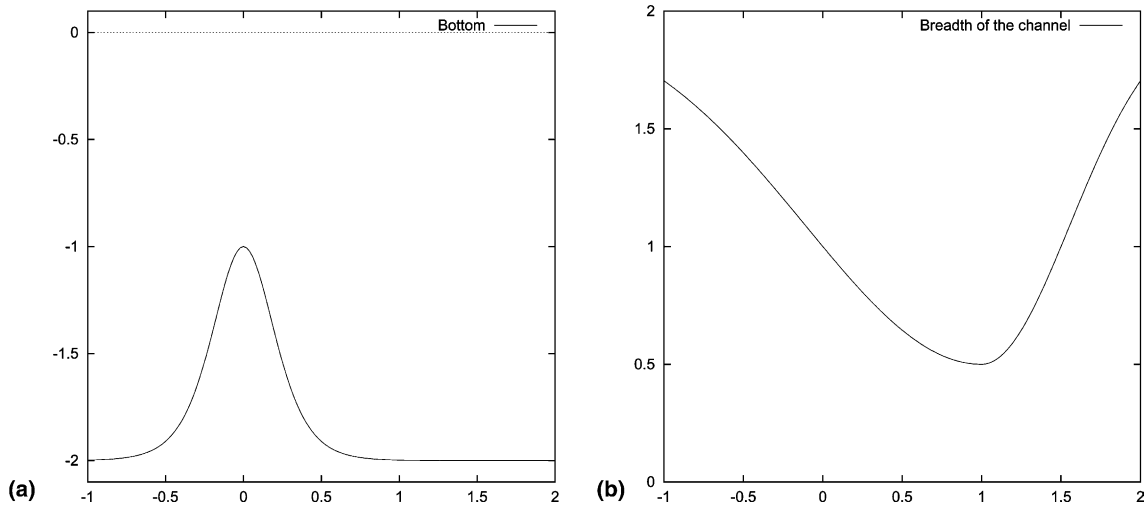

Fig. 8. Channel geometry: depth and breadth. (a) Channel topography and (b) channel breadth.

as boundary conditions, where q_1^{R}, q_2^{L} and q_2^{R} are the discharges corresponding to a given submaximal stationary GA&F solution. The CFL parameter used in this experiment is 0.7.

Figs. 9(a) and (b) show, respectively, the initial and the final stationary states reached in the experiment performed. In Fig. 9(b), the final state is compared with the corresponding GA&F approximate solution.

5.4. Application to the Strait of Gibraltar

In this last paragraph the model is applied to the simulation of the exchange flow through the Strait of Gibraltar. Two numerical experiments are presented. The aim of the first one is to obtain a steady-state solution representing the secular exchange flow through the Strait of Gibraltar when no forcing is applied. This is done by performing a lock-exchange experiment. The goal of the second experiment is to study tidal effects on the exchange flow and on the behaviour of the interface. This is done by taking first experiment steady-state solution as initial condition and imposing the tidal forcing through an adequate choice of boundary conditions. Animations corresponding to both experiments can be found at http://www.dam-flow.org.

To perform these experiments the real geometry of the Strait is approached by constructing appropriate breadth and bottom functions. To do so, we use bathymetric and coast line data and construct from them an "equivalent symmetric channel" approximating the actual topographic characteristics of the Strait of Gibraltar. This is done as follows: First an axis defining the Strait orientation is settled. Along this axis we consider $M = 200$ transversal cross-sections, S_i, $i = 1, \ldots, M$, whose areas are numerically computed. This spatial discretization corresponds to a $\Delta x \approx 600$ m. The bottom depth, at each of these sections, is taken as the maximal depth, b_i, found in the bathymetric data. Finally, at each cross-section, channel breadth is approximated by a continuous piecewise linear function constructed in such a way that the cross-section areas are preserved. Figs. 10(a) and (b) show the bottom function and the breadth at the top of the channel obtained by this procedure. In the figures, the Atlantic Ocean is located to the left and the Mediterranean Sea to the right. Fig. 11 depicts the cross-sections corresponding to the shallowest (Camarinal Sill) and the narrowest (Tarifa Narrows) sections, and to the open boundary sections corresponding to Trafalgar C.-Spartel C. section (left) and Punta Carnero-Ceuta section (right), respectively. In Fig. 12 real

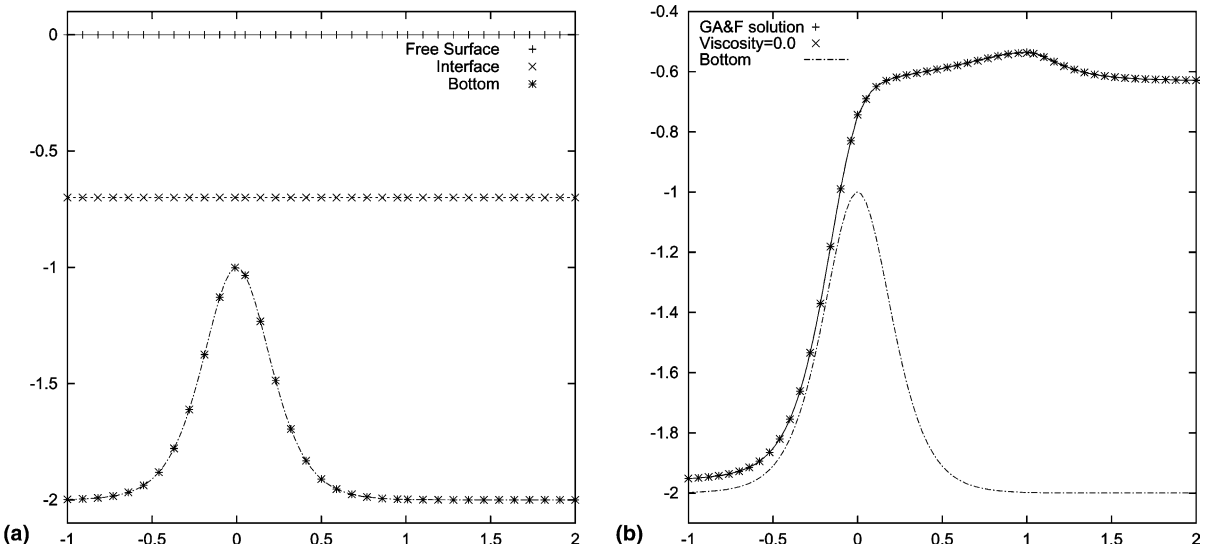

Fig. 9. Stationary solution and generalized A&F solution. (a) Initial condition and (b) stationary solution and GA&F solution.

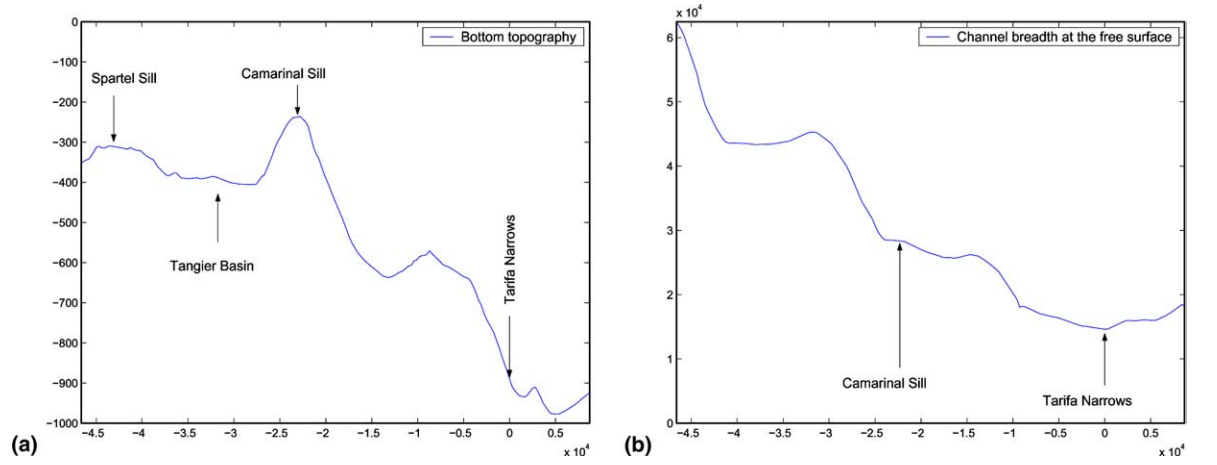

Fig. 10. Geometry of the channel (Strait of Gibraltar). (a) Bottom topography and (b) channel breadth at surface.

cross-sections corresponding to Camarinal Sill and Tarifa Narrows and their symmetric approximations are compared. The location of these two sections are also marked in Fig. 10(a).

5.4.1. The secular exchange: maximal steady-state solution

The objective of this experiment is the obtaining of a steady-state solution that represents the secular exchange in the sense of *Armi and Farmer* theory ([1–3,9]). This solution will also provide an initial condition for further numerical experiments, here for the tidal forced simulation. To obtain this solution a lock-exchange experiment is newly performed. Fig. 13(a) shows the initial condition: The Atlantic waters, on the left, are separated from the Mediterranean denser waters by an artificial dam. The ratio of densities is equal to 0.99805. Newly the relationship $Q_1 = -Q_2$ is imposed at the boundaries and CFL = 0.5.

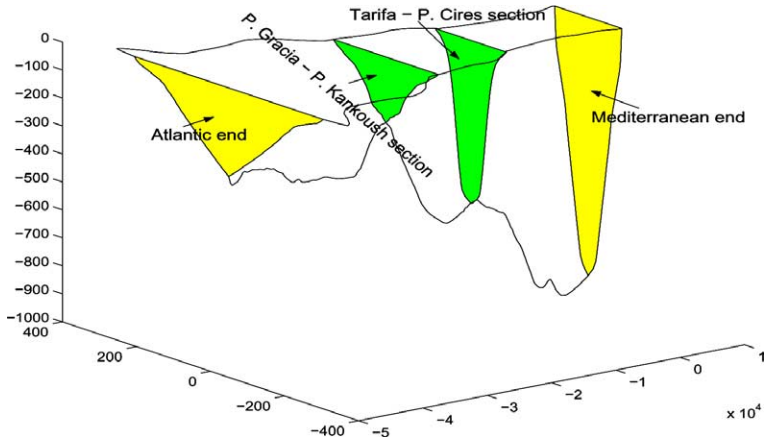

Fig. 11. Some relevant sections in the Strait of Gibraltar.

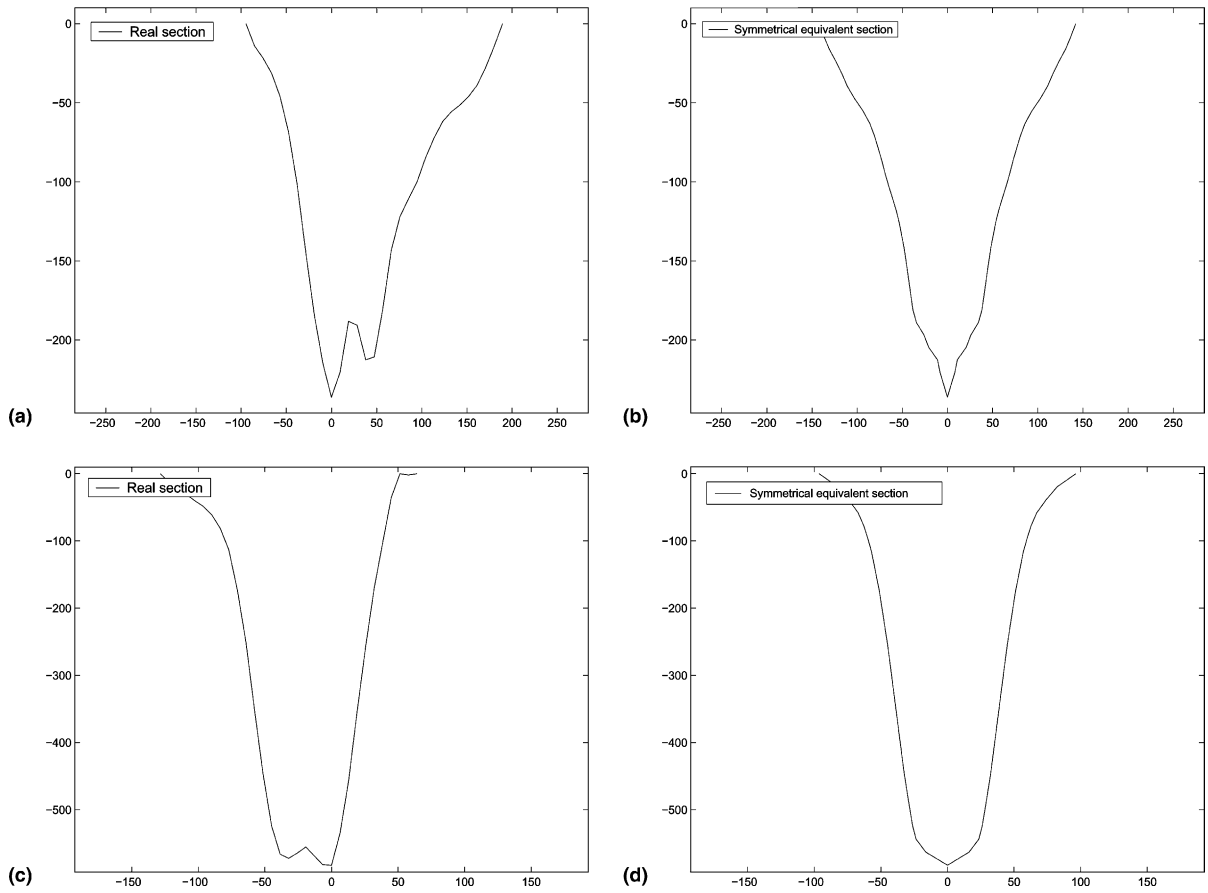

Fig. 12. Camarinal Sill and Tarifa Narrows sections. Real (left) and symmetric equivalent ones (right). (a) Real cross-section at Camarinal Still; (b) symmetric equivalent section at Camarinal Still; (c) real section at Tarifa Narrows; (d) symmetric equivalent section at Tarifa Narrows.

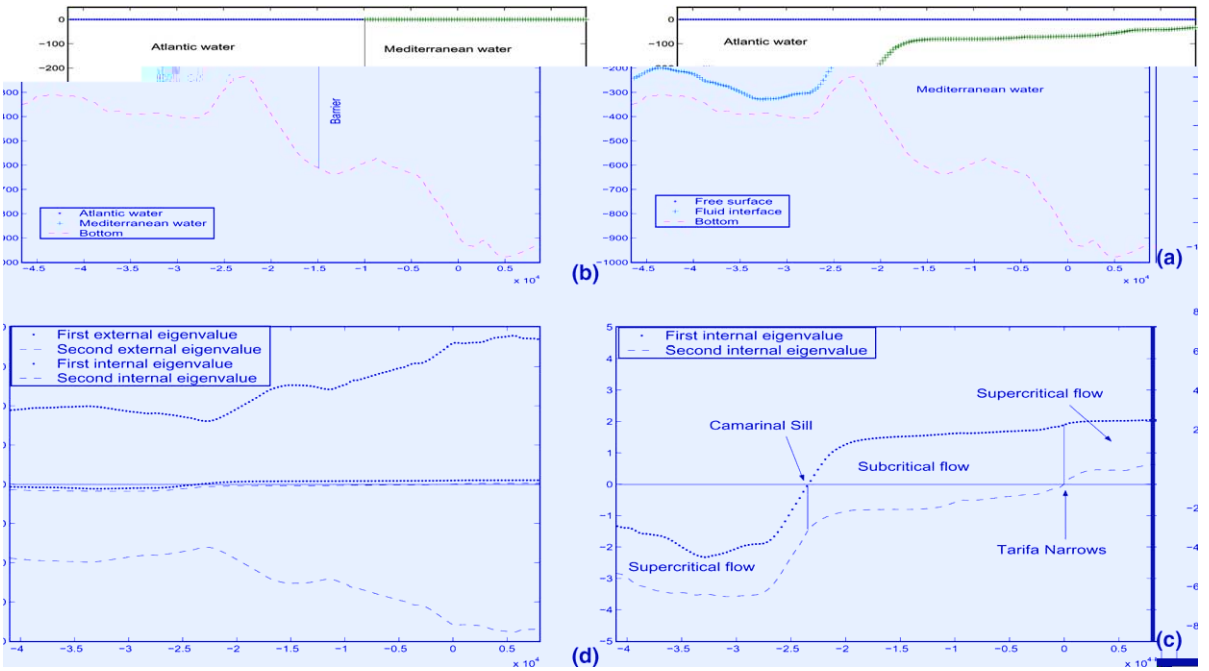

Fig. 13. Lock-exchange experiment: Initial conditions and maximal stationary exchange flow reached. (a) Initial conditions; (b) free surface and interface; (c) internal and external eigenvalues; (d) internal eigenvalues.

Fig. 13(b) depicts the interface and free surface of the steady state reached. The discharge is $Q_1 = -Q_2 = 0.855$ Sv, magnitude that agrees with some experimental data (see, for example, [6])

To analyse the nature of the flow we can look at the eigenvalues of the computed solution. Figs. 13(c) and (d) show, respectively, the four eigenvalues and the two internal eigenvalues corresponding to the steady-state solution along the Strait. It can be observed the presence of a subcritical region bounded by two sections where one of the two internal eigenvalues takes the value zero. One of these sections is located near Camarinal Sill and the other one at Tarifa Narrows. Out of this subcritical region, the two internal eigenvalues have the same sign and therefore the flow is supercritical. In the framework of the hydraulic theory developed by *Armi and Farmer*, this subcritical region is called a '*control region*' and the two critical sections bounding it are called '*control sections*'. In the case of a channel with a simple geometry composed by a combination of an offset sill and narrows, when a control region is present, the exchange rate is fully defined without reference to reservoirs conditions. When this occurs, the flow regimen established is referred to as *maximal exchange*. When a maximal flow occurs, in the sense defined above, the exchange rate is greatest, which motivates its name. As pointed out above, in the numerical experiment presented here the same configuration with the presence of a control region is found for the more complex geometry of a channel that has been considered to represent the Strait of Gibraltar. In this sense, the simulated flow represents a maximal exchange.

If we compare Fig. 13(b) with the hypothetical steady state proposed in *Armi and Farmer* [3], it can be observed that both figures agree for the location of the interface to the east of Camarinal Sill and to the west of Spartel Sill, being the flow supercritical in both regions, but they differ in the region between these two locations. In [3], the steady state proposed exhibits a control section placed at Spartel Sill and an internal hydraulic jump which are not present in the computed solution. Later on, we will come back to this discussion.

5.4.2. Tidal simulation

In order to study the essential elements of the time dependent response in the Strait of Gibraltar to tidal forcing, the next numerical experiment consists in a simulation of the main semidiurnal (M2 and S2) and diurnal (O1 and K1) tidal waves in this narrows. The numerical experiment has been designed as follows: Using the steady-state solution reached at the previous lock-exchange experiment as initial condition, the model is integrated over 30 semidiurnal tidal cycles to achieve a stable quasi-time-periodic solution. The model is forced at the open boundaries with boundary conditions that simulate the four main tidal components to be considered (M2, S2, O1 and K1):

$$h_1(x_B,t)+h_2(x_B,t)=\bar{h}_B-\sum_{n=1}^{4}Z_n(x_B)\cos(\alpha_n t-\phi_n(x_B)).$$

Here x_B represents a point of the open boundaries (left or right); $Z_n(x_B)$ and $\phi_n(x_B)$ are the prescribed surface elevation amplitudes and phases of the nth tidal constituent at the boundary sections; α_n its frequency, $\bar{h}_B$ the total depth of the water column corresponding to the steady-state solution at this boundary. The M2, S2, O1 and K1 tidal elevation amplitudes, phases and frequencies used here were obtained by interpolating the measured data at the coastal stations of Trafalgar and Spartel (on the western end) and the coastal stations of Punta Carnero and Ceuta (on the eastern end) obtained by García-Lafuente et al. [10]. Once the quasi-time-periodic regime is established, the model is integrated for another 29-day period. Thereafter an harmonic analysis is performed on the tidal elevation over this 29-day period in order to compare the results with the measured data provided by García-Lafuente et al. [10] at some relevant points. The comparison between observed and numerical data are presented in Tables 1 and 2 where phases are related to the M2 tide.

As it can be observed, the maximum differences do not exceed 3.0 cm (that is, about 5% in relative units) for the M2 and S2 amplitudes and 2° for their phases. The agreement between observed and predicted tidal constants for the O1 and K1 tidal components is not as good as for the M2 and S2 constituent. This is due, on the one hand, to the fact that 2D effects are stronger on the O1 and K1 tidal waves, as it can be seen in their phases chart (see [10]). Therefore, a 2D model including Coriolis effects must be used for a better simulation of these effects. On the other hand, the diurnal tides (O1 and K1) are very sensitive to small variations of the bottom morphology (see [20]). As a consequence, a more precise representation of the topography would also be necessary.

Table 1
Tarifa – Punta Cires section

	M2		S2		K1		O1	
	Obs	Pred	Obs	Pred	Obs	Pred	Obs	Pred
Amplitude (cm)	38.94	39.88	14.13	14.85	2.73	2.16	0.84	0.87
Phase (°)	0	0	27.75	26.07	80.25	77.21	ND	ND

Table 2
Punta Gracia – Punta Kankoush section

	M2		S2		K1		O1	
	Obs	Pred	Obs	Pred	Obs	Pred	Obs	Pred
Amplitude (cm)	57.7	55.15	21.5	20.08	3.8	1.22	2.25	3.11
Phase (°)	0	0	22.37	24.33	22.75	−16.01	262.91	198.58

Fig. 14 shows the evolution of the free surface elevation at Tarifa Narrows given by the model during the 29-day tidal forcing experiment. Notice that, as expected, the model reproduces at this location two periods of spring tides and other two periods of neap tides, in agreement with the boundary conditions imposed.

In Fig. 15 the free surface and the interface at twelve different stages (separated by 1 h time) of a semidiurnal tidal cycle corresponding to a spring tide are depicted. In Fig. 16 the composite Froude number at the same tidal stages are shown. The starting and final points of this time-series, located at the day 18 of the simulated period, are marked with stars in Fig. 14. The sequence of figures shown here can be compared with the essential elements of the time dependent response in the Strait of Gibraltar summarized by Armi and Farmer [3]. We will focus on the four synopses presented by these authors, that summarized the analysis of an extensive campaign carried out in April 1986. Nevertheless, they present a much detailed description of the processes sketched in their schematic diagrams.

Fig. 15(b) corresponds to conditions 2 h before *High Water*. In order to clearly identify the nature of the flow, Fig. 16(b) depicts the value of the composite Froude number along the Strait. The flow is controlled at Spartel Sill (located at $x = -4.5 \times 10^4$ in the figure). At this time of the tidal period the interface in the Tangier Basin is rising (see Figs. 15(a)–(e) to appreciate this fact) because of the strong westward flow of Mediterranean water over Camarinal Sill at a speed of about 1.46 m/s (in agreement with the 1.4 m/s provided by Armi and Farmer [3]). Just west of Camarinal Sill there is a large bore matching the supercritical flow on the western flank of the sill with the subcritical flow in Tangier Basin. The flow is newly controlled slightly to the west of Camarinal Sill (located at $x = -2.3 \times 10^4$ in the figure), being subcritical at the Sill and to its east. Just west of Tarifa Narrows ($x = 0$) the interface deepens slightly and a third control point is found, being the flow supercritical to the east.

Figs. 15(d) and 16(d) show conditions at *High Water*. In this case the flow is subcritical over Spartel Sill and over Camarinal Sill, being the controls located one slightly west of Spartel Sill, another one to the east of Camarinal Sill. The flow is subcritical in the Tangier Basin which, at this stage of the tide period, is being filled with Mediterranean water. This Basin continues further filling (see Fig. 15(e) corresponding to 1 h later). At that time the small supercritical region located west of Camarinal Sill becomes subcritical and only two control sections are present. The computed first layer water velocity obtained at Camarinal Sill agrees with the observations of [3] (0.12 vs. 0.1 m/s), being too strong the computed velocity obtained for the second layer (−1.18 vs. −0.7 m/s). To get model velocity values closer to the observed ones, friction effects must be included into the numerical model. It can be observed in Figs. 15(d) and (e) (and in all the intermediate snapshots not shown here) how the large bore that was previously formed to the west of Camarinal Sill propagates east down the Strait towards Tarifa Narrows. Following the synopsis presented by Armi and Farmer [3], at High Water the flow in the Strait should have just two controls: one at Spartel West and another one at Tarifa Narrows, being the flow subcritical all along the Strait. This is not the case for the numerical experiment presented here where the flow is controlled to the east of Camarinal Sill

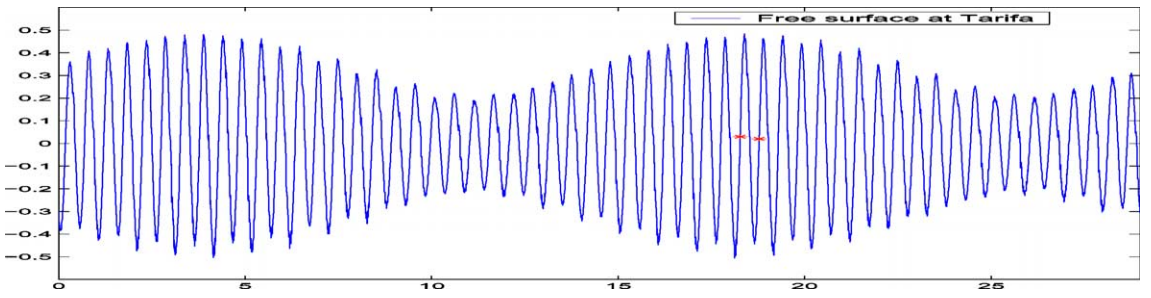

Fig. 14. Simulated free surface elevation (in m) at Tarifa Narrows during the tidal forcing (29 days).

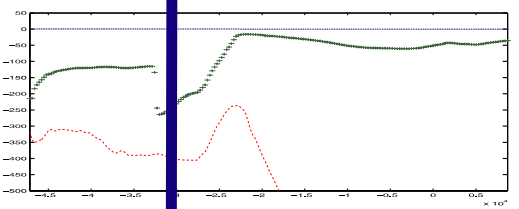
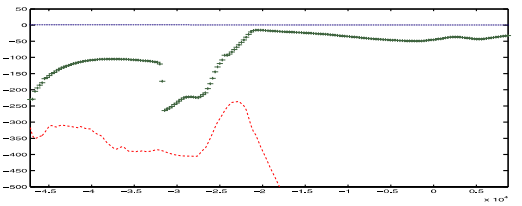
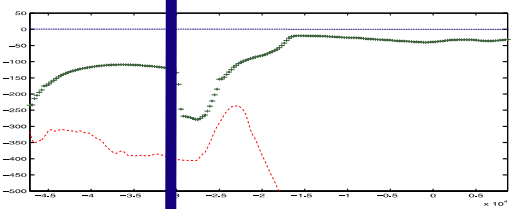
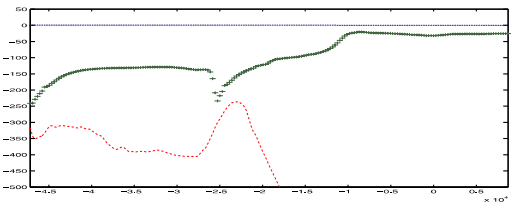
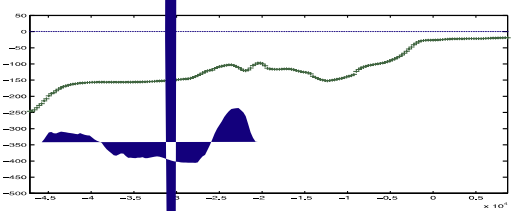

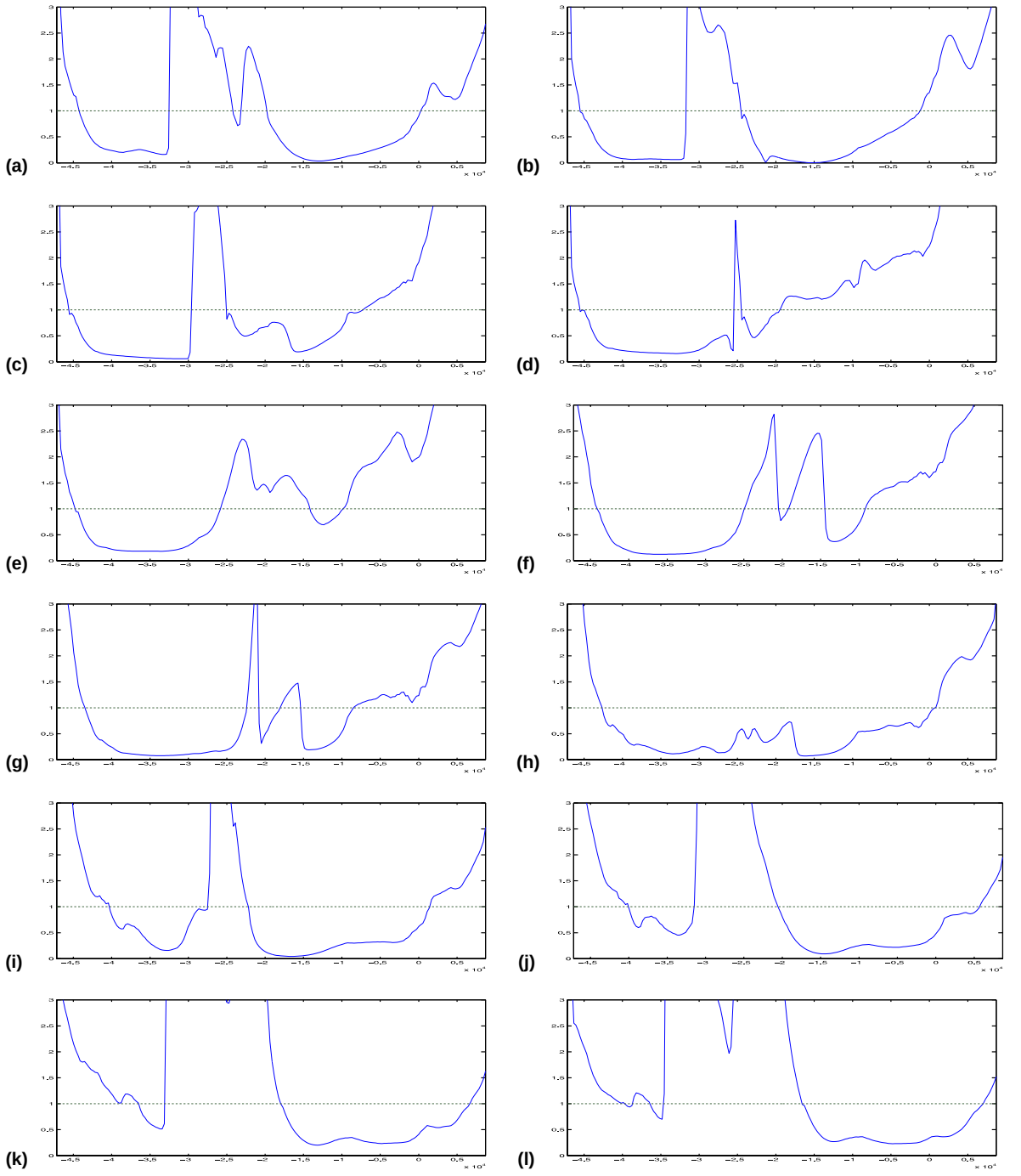

Fig. 16. Composite Froude number (in solid line) during a semidiurnal tidal cycle at the Strait of Gibraltar. (a) $t = 439$ h; (b) two hours before the High Water ($t = 440$ h); (c) $t = 441$ h; (d) High Water ($t = 442$ h); (e) $t = 443$ h; (f) $t = 444$ h; (g) $t = 445$ h; (h) two hours before Low Water ($t = 446$ h); (i) $t = 447$ h; (j) Low Water ($t = 448$ h); (k) $t = 449$ h; (l) $t = 450$ h.

remaining supercritical to the east of this control (see Figs. 15(d) and 16(d)). In the tidal cycle picked here for its analysis and description, a situation as the one described in [3] for High Water conditions can be found closer to Low Water (see the description for conditions 2 h before Low Water). Periods of about 1 h wherein only two controls are present appear once per tidal cycle, for spring tides. These two controls are located at Spartel Sill and at Tarifa Narrows, respectively, being the flow subcritical between these two locations, as in the High Water synopsis presented by *Armi and Farmer*. The moment at which this situation occurs is progressively closer to High Water as the amplitude of the tide decreases. For neap tides this happens at High Water or at very close times.

Fig. 15(h) corresponds to conditions 2 h before *Low Water*. At this time of the tidal period Tangier Basin is draining Mediterranean water (see Figs. 15(g)–(j) to make out this process). This is due to the much higher outflowing flow of Mediterranean water through Spartel Sill than the inflowing flow through Camarinal Sill. This could even produce a reversal of the Mediterranean flow at Camarinal Sill, as it is the case here, where the computed velocity of the Mediterranean flow at Camarinal Sill is +0.18 m/s (vs. +0.20 measured by Armi and Farmer [3]) and −1.59 m/s at Spartel Sill (vs. −1.4 in [3]). In this case only two controls located at Spartel Sill and at Tarifa Narrows, respectively, are present (see Fig. 16(h)). The flow is subcritical between these two locations and supercritical outside this control region.

Fig. 15(j) shows conditions at *Low Water*. The flow is controlled to the east of Spartel Sill (see Fig. 16(j)). The Mediterranean flow continues outflowing at this location at a high rate (at a velocity between −2.14 and −1.79 m/s, depending on the location), which made the progressive lowering of the interface up to this stage of the tidal period. But is at this point of the tidal period where Tangier Basin stops draining Mediterranean water: Although the outflowing rate at Spartel is high, the Mediterranean water coming into the Tangier Basin through Camarinal Sill do so as a highly supercritical flow that compensates the lose through Spartel. The highly supercritical Mediterranean input flow through Camarinal produces, in its turn, the formation of a large bore (see also subsequent figures to appreciate the growing of the bore) that connects the supercritical region formed as consequence of the strong Mediterranean flow with the subcritical region located in the western part of the Tangier Basin. The bore is progressively growing and moving westwards the Tangier Basin (see Figs. 15(j)–(l)). The mechanism just described produces the filling of the Tanger Basin with Mediterranean water, reversing the former draining conditions. The flow velocities computed by the model at Spartel Sill and Camarinal Sill are −1.79 m/s (vs. −1.8 m/s measured by Armi and Farmer [3]) and −1.53 (vs. −1.2 m/s), respectively, at these two locations. Nevertheless, it must be pointed out the large fluctuations in the magnitude of the velocities in such a critical point as Camarinal Sill. As example, in this case, the computed velocities for the Mediterranean flow were of −2.25, −1.53 and −0.95 m/s at three close locations: slightly west of the sill, at the sill, and slightly east of the sill, respectively. At this stage of the tide, the Atlantic flow is reversed over Camarinal Sill (the computed velocity is −0.67 vs. −0.5 m/s measured by Armi and Farmer [3]), as the large pool of Atlantic water in the subcritical portion between Camarinal Sill and Tarifa Narrows (see Fig. 15(i) 1 h before) spreads out both to east and west. A new control appears when the interface rises east of Tarifa Narrows being the flow supercritical to the east of the control.

Through the simulation it can be observed that Tangier Basin acts as a reservoir that fills and drains on each tidal cycle. The brief description of the process is as follows: At spring tides about 1 h after High Water, when Tangier Basin has been filling and the interface there has raised, the moving control close to Camarinal Sill is lost. This happens for about 1 h. For neap tides this occurs closer or at High Water conditions and the lose control situation lasts longer, for about 3 h. Then, the Tangier Basin starts draining, first due to the reversal of the Mediterranean flow at Camarinal Sill (Figs. 15(f)–(h)) and later on for a larger Mediterranean outflowing flow through Spartel Sill than the incoming flow though Camarinal Sill (Fig. 15(i)) this makes the interface to drop below the interface level east of Camarinal Sill. The large amount of Mediterranean water incoming through Spartel Sill makes that the moving control close to Camarinal Sill is re-established. Meanwhile, the interface behaves in a complex manner (this can be

observed plotting more intermediate snapshots or making an animation of the simulation). About 1 h before Low Water, the increasingly larger and progressively more supercritical flow of Mediterranean water entering through Camarinal Sill into the Tangier Basin initiates the formation of a bore west of Camarinal Sill. The bore initially grows up to occupy half of the Tangier Basin, remaining there for about half of the tidal cycle when a new refilling of the basin makes the bore move eastwards and latter, when the control is again lost in a new tidal cycle, makes it dissappear propagating east of the sill.

East of Camarinal Sill, between the sill and the contraction, there is another fluctuating reservoir of water. In this case it is the Atlantic water that fills or drains from this reservoir of the Strait. Just as Tangier Basin can drain from both ends on a falling tide, so does the pool of Atlantic water east of Camarinal drain from both ends, west over Camarinal Sill and east through Tarifa Narrows, on a rising tide.

To conclude our analysis, we come back to the hypothetical steady state representation of the Mediterranean and Atlantic water interface proposed by Armi and Farmer [3]. To interpret this representation we have computed the mean location of the interface during the 29-day tidal forcing simulation presented above. Fig. 17 depicts the mean interface. The agreement between the mean interface of the tidal simulation presented here and the hypothetical steady state proposed by *Armi and Farmer* is good along all the Strait in contrast with the maximal steady-exchange solution. It should be observed that this mean interface is not a solution of the numerical model, as this it is not linear. As a consequence, even if the model is initialized with a maximal steady-state solution, as is was done here, once a tidal forcing is applied, the resulting solution turns around a 'mean state' that presents the main features predicted in [3]. The mean values of the discharges averaged over the 29-day tidal forcing simulation are of 1.0923 Sv for the upper layer and of -1.0327 Sv for the second layer. Observe that these values are larger than the values computed for the maximal exchange solution with $q_r = 1$ that were $Q_1 = -Q_2 = 0.855$ Sv. Even if the simulation were initialized from a maximal solution with $q_r = 1.0$, through the tidal cycle the Atlantic flow becomes larger than the mean Mediterranean flow. Therefore if other effects, such as evaporation, were not present the Mediterranean Sea would finally be filled with Atlantic water. Notice that the structure of the maximal exchange solution previously computed is lost when the tidal forcing is introduced. All along the tidal simulation the supercritical nature of the flow at both bounding sections of the Strait is always preserved, but the flow that connects these two supercritical regions is highly time dependent and the behaviour of the interface is complex. Bores develop and the control at Camarinal Sill is periodically lost. From a qualitative point of view, the model solution agrees well with the observations and analysis performed by Armi and Farmer [3].

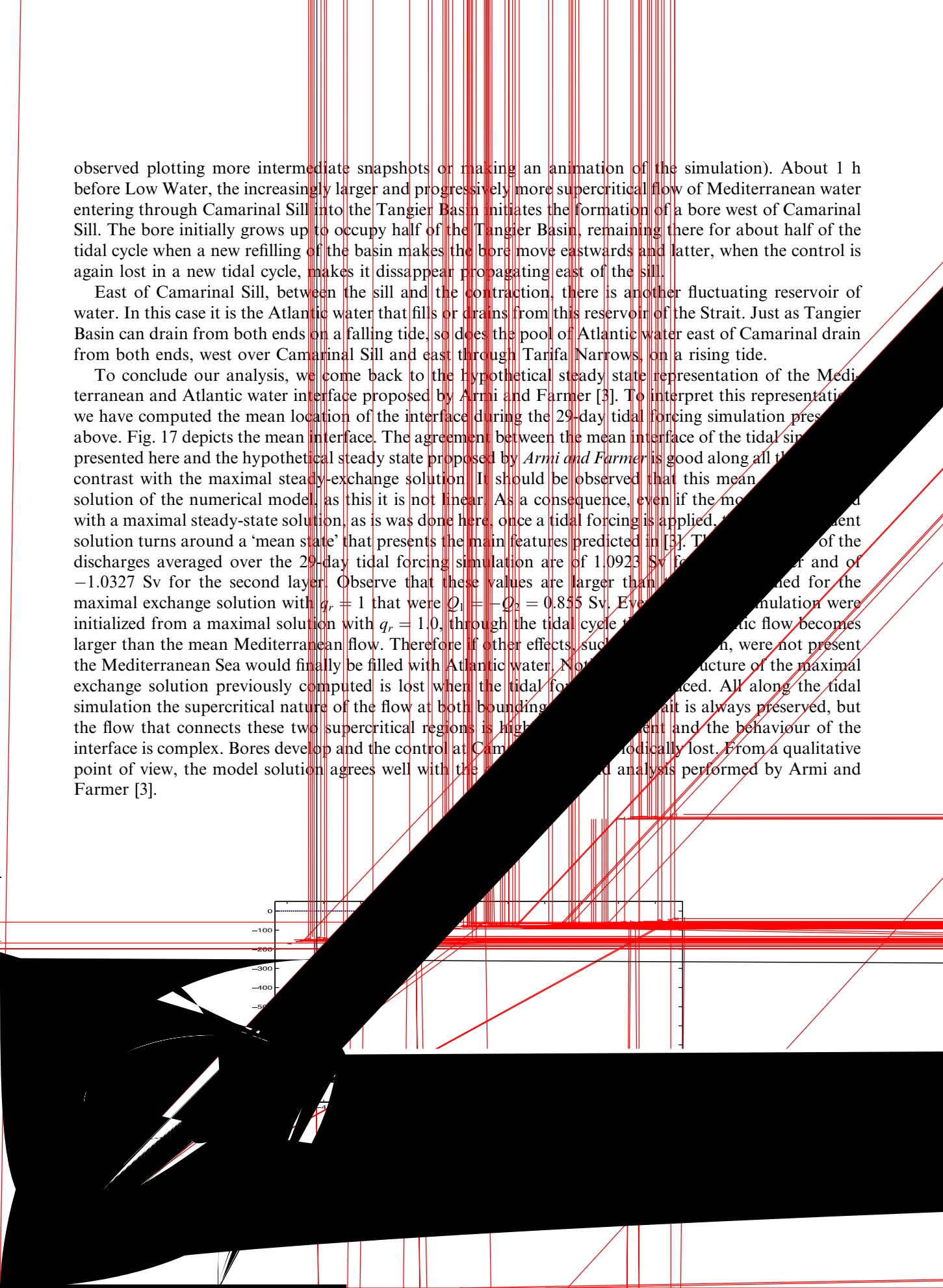

6. Conclusions

In this work, a formulation of the two layer Shallow Water Equations for channels with irregular geometry under the form of two coupled systems of conservation laws with source terms have been derived and a generalized Q-scheme for solving the system with a suitable treatment of the coupling and source terms has been proposed. The particular expressions for the generalized Q-schemes of Roe and Van Leer have also been provided. The extension of the enhanced consistency condition introduced in [4] to the proposed numerical schemes has been done, and a result that gives some conditions to ensure that a generalized Q-scheme satisfies this property has been proved. It has been also checked that this property is satisfied in practice and that no spurious waves appear as consequence of the discretization of the source terms.

Model performance has been assessed by comparing the numerical results with the analytical solutions provided by *Armi and Farmer* for channels with rectangular cross-sections and simple geometries. We have also been able to properly simulate maximal exchange solutions by solving the classical lock exchange problem without adding any viscous term in the mathematical model as it is common practice when dealing with this problem.

Finally, the model has been used to simulate the flow exchange through the Strait of Gibraltar. To do so, an equivalent symmetric channel approaching the real geometry of the Strait has been constructed and a steady-state solution has been computed starting from *lock-exchange* initial conditions. This solution, that represents the secular exchange through the Strait, presents the main features predicted by the hydraulic theory developed by *Armi and Farmer*. Moreover, the discharge obtained agrees quite closely with experimental measurements. Next, the main semidiurnal and diurnal tidal waves in the Strait of Gibraltar have been simulated by imposing the effect of the tides through the boundary conditions at the two open boundaries. In despite of the simplifications of the model (mainly due to its one-dimensional character), the agreement with measurements (at least for the semidiurnal tides) is quite good. The development of internal bores travelling westward and eastward are well simulated. The numerical experiment presented here has revealed a complicated pattern of time dependent hydraulics fluctuations involving changing interfacial levels and moving control points at different stages of the tide, being these patterns in good agreement with the analysis of observed data performed in [3]. Therefore, these results seems to confirm that this approach is well suited for oceanographical purposes and, in particular, for a realistic simulation of flows through the Strait of Gibraltar.

Acknowledgements

This research has been partially supported by the C.I.C.Y.T. (Project REN2000-1168-C02-01). Thanks to Alfredo Izquierdo for providing us the bathymetric data for the Strait of Gibraltar and to E. Toro for his comments. Finally, we acknowledge all of our referees for their very useful comments that helped us to improve the original manuscript.

References

[1] L. Armi, The hydraulics of two flowing layers with different densities, J. Fluid Mech. 163 (1986) 27–58.
[2] L. Armi, D. Farmer, Maximal two-layer exchange through a contraction with barotropic net flow, J. Fluid Mech. 164 (1986) 27–51.
[3] L. Armi, D. Farmer, The flow of the mediterranean water through the strait of gibraltar. The flow of the atlantic water through the strait of gibraltar, Prog. Oceanogr. 21 (1988) 1–105.
[4] A. Bermúdez, M.E. Vázquez, Upwind methods for hyperbolic conservation laws with source terms, Comput. Fluids 23 (8) (1994) 1049–1071.

[5] A. Bermúdez, A. Dervieux, J.A. Désidéri, M.E. Vázquez, Upwind schemes for the two-dimensional shallow water equations with variable depth using unstructured meshes, Comput. Methods Appl. Mech. Engrg. 155 (1–2) (1998) 49–72.
[6] H. Bryden, J. Candela, T.H. Kinder, Exchange through the Strait of Gibraltar, Prog. Oceanogr. 33 (1994) 201–248.
[7] M.J. Castro, J. Macías, C. Parés, A *Q*-scheme for a class of systems of coupled conservation laws with source term. Application to a two-layer 1-D shallow water system, Math. Model. Numer. Anal. 35 (1) (2001) 107–127.
[8] M.J. Castro, J. Macías, C. Parés, J.A. Rubal, M.E. Vázquez-Cendón, Two-layer numerical model for solving exchange flows through channels with irregular geometry, in: Proceedings of "ECCOMAS 2001", Swansea, 2001.
[9] D. Farmer, L. Armi, Maximal two-layer exchange over a sill and through a combination of a sill and contraction with barotropic flow, J. Fluid Mech. 164 (1986) 53–76.
[10] J. García Lafuente, J.L. Almazán, F. Castillejo, A. Khribeche, A. Hakimi, Sea level in the strait of Gibraltar: tides, Int. Hydrogr. Rev. LXVII (1) (1990) 111–130.
[11] P. García-Navarro, M.E. Vázquez-Cendón, On numerical treatment of the source terms in the shallow water equations, Comput. Fluids 29 (8) (2000) 17–45.
[12] A. Harten, On a class of high resolution total-variation-stable finite-difference schemes, SIAM J. Numer. Anal. 21 (1) (1984) 1–23.
[13] K.R. Helfrich, Time-dependent two-layer hydraulic exchange flows, J. Phys. Oceanogr. 25 (3) (1995) 359–373.
[14] A. Izquierdo, L. Tejedor, D.V. Sein, J.O. Backhaus, P. Brandt, A. Rubino, B.A. Kagan, Control variability and internal bore evolution in the Strait of Gibraltar, Estuarine Coastal Shelf Sci. 53 (2001) 637–651.
[15] G.A. Lawrence, The hydraulics of steady 2-layer flow over a fixed obstacle, J. Fluid Mech. 254 (1993) 605–633.
[16] J. Macías, Approximate Armi and Farmer solutions for flows through arbitrary channels, Internal Journal 0115 group on "Differential Equations Numerical Analysis and Applications", University of Málaga, Spain, 2001.
[17] P.L. Roe, Approximate Riemann solvers parameter vectors and difference schemes, J. Comput. Phys. 43 (1981) 357–371.
[18] P.L. Roe, Upwinding differenced schemes for hyperbolic conservation laws with source terms, in: C. Carasso, P.-A. Raviart, Serre (Eds.), Proceedings of the Conference on Hyperbolic Problems, Springer, Berlin, 1986, pp. 41–51.
[19] J.B. Schijf, J.C. Schonfeld, Theoretical considerations on the motion of salt and fresh water, in: Proceedings of the Minn. Int. Hydraulics Conv., Joint meeting IAHR and Hyd. Div. ASCE., September 1953, pp. 321–333.
[20] L. Tejedor, A. Izquierdo, D.V. Sein, B.A. Kagan, Tides and tidal energetics of the Strait of Gibraltar: a modeling approach, Tectonophysics 294 (1998) 333–347.
[21] E.F. Toro, Riemann Solvers and Numerical Methods for Fluid Dynamics. A Practical Introduction, Springer, 1997.
[22] E.F. Toro, M.E. Vázquez-Cendón, Model hyperbolic systems with source terms: exact and numerical solutions, in: Proceedings of "Godunov methods: Theory and Applications", 2000.
[23] B. van Leer, Towards the ultimate conservative difference scheme III. Upstream-centered difference schemes for ideal compressible flow, J. Comput. Phys. 23 (1977) 263–275.
[24] B. van Leer, Progress in multi-dimensional upwind differencing. ICASE Report 92/43, NASA Langley Research Center, Hampton, VA, 1984, in: Proceedings of the 13th International Conference on Numerical Methods in Fluid Dynamics, Rome, 1992.
[25] M.E. Vázquez-Cendón, Estudio de Esquemas Descentrados para su Aplicación a las leyes de Conservación Hiperbólicas con Términos Fuente, PhD thesis, Universidad de Santiago de Compostela, 1994.
[26] M.E. Vázquez-Cendón, Improved treatment of source terms in upwind schemes for the shallow water equations in channels with irregular geometry, J. Comput. Phys. 148 (1999) 497–526.